



AMERICAN UNIVERSITY OF BEIRUT

NON-DESTRUCTIVE EVALUATION OF MIXING AND  
DEFECTS OF FRICTION STIR WELDED DISSIMILAR AA6061-  
T6 AND AZ31B BY X-RAY COMPUTED TOMOGRAPHY.

by

AHMAD MOHAMMAD-RABIEH BAYDOUN

A thesis  
submitted in partial fulfillment of the requirements  
for the degree of Master of Engineering  
to the Department of Mechanical Engineering  
of the Maroun Semaan Faculty of Engineering and Architecture  
at the American University of Beirut

Beirut, Lebanon  
August 2019

AMERICAN UNIVERSITY OF BEIRUT

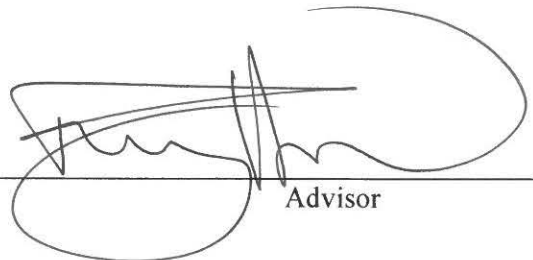
NON-DESTRUCTIVE EVALUATION OF MIXING AND  
DEFECTS OF FRICTION STIR WELDED DISSIMILAR AA6061-  
T6 AND AZ31B BY X-RAY COMPUTED TOMOGRAPHY.

by

AHMAD MOHAMMAD-RABIEH BAYDOUN

Approved by:

Dr. Ramsey Hamade, Professor  
Mechanical Engineering



Advisor

Dr. Mu'Tasem Shehadeh, Associate Professor  
Mechanical Engineering



Member of Committee

Dr. Lamya Ann Atweh, Assistant Professor  
Diagnostic Radiology



Member of Committee

Date of thesis defense: August 9, 2019

AMERICAN UNIVERSITY OF BEIRUT

THESIS, DISSERTATION, PROJECT RELEASE FORM

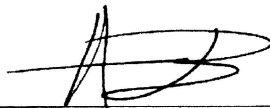
Student Name: Baydoun Ahmad Mohammad-Rabieh  
Last First Middle

Master's Thesis  Master's Project  Doctoral Dissertation

I authorize the American University of Beirut to: (a) reproduce hard or electronic copies of my thesis, dissertation, or project; (b) include such copies in the archives and digital repositories of the University; and (c) make freely available such copies to third parties for research or educational purposes.

I authorize the American University of Beirut, to: (a) reproduce hard or electronic copies of it; (b) include such copies in the archives and digital repositories of the University; and (c) make freely available such copies to third parties for research or educational purposes after:

- One ---- year from the date of submission of my thesis, dissertation, or project.
- Two ---- years from the date of submission of my thesis, dissertation, or project.
- Three ---- years from the date of submission of my thesis, dissertation, or project.

  
\_\_\_\_\_  
Signature

September 16, 2019  
\_\_\_\_\_  
Date

## ACKNOWLEDGMENTS

الحمد لله

Deepest thanks to Prof. Hamade for his unwavering support and guidance, his constant drive to research and innovate is genuinely inspiring. A special thanks to the thesis committee members Prof. Mu'Tasem Shehadeh and Prof. Lamyia Ann Atweh for their insight and feedback. Thank you to the Engineering Faculty and Mechanical Engineering Department.

The author would like to thank the radiology department at the American University of Beirut Medical Center (AUBMC), the Central Research Science Laboratory (CRSL) and the Engineering Shops, for their technical help.

The author acknowledges the financial support of the University Research Board (URB) at the American University of Beirut.

A special thanks to my family and most importantly my mother, without which none of my academic achievements would have been possible. Overcoming all the challenges a single mother faces in this modern world she raised me to become the man I am today.

# AN ABSTRACT OF THE THESIS OF

Ahmad Mohamad Rabieh Baydoun for

Master of Engineering

Major: Mechanical Engineering

Title: Non-Destructive Evaluation of Mixing and Defects of Friction Stir Welded Dissimilar AA6061-T6 And AZ31b By X-Ray Computed Tomography.

Friction stir welding (FSW) is a relatively new manufacturing process employed in the production of parts and components for numerous heavy machinery, including cars planes and spacecrafts. The analysis of welds produced by this method is critical for the safe and successful operation of these devices. Non-destructive testing (NDT) techniques offer a way to evaluate the welds while preserving the specimen. Traditional NDT methods focused on the detection of internal defects and their effect on the weld strength. Ultrasonic, X-ray, Gamma-ray, and other scanning technologies have been employed to analyze these internal defects. The evaluation of material mixing in the thermally and thermally-mechanically affected weld zones (TAZ TMAZ) is a less researched area due to the inability of traditional testing techniques in detecting different materials accurately and in a non-destructive manner. Since having a more homogeneous weld zone will lead to enhanced mechanical properties, having a systematic method to analyze material mixing is highly sought after.

In this research, a method for material flow analysis and defect detection by based on computed tomography X-ray (CT X-ray) scans is presented, tested, and corroborated. First dissimilar friction welded AA6061T6/AZ31b welds are produced. The welded samples are then analyzed using the proposed NDT CT X-ray method. Based on the Hounsfield Units values (HU), the CT X-ray scans are segmented using the global Otsu thresholding method into masks for each different material, and 3D renderings are generated. Measurements of materials penetration and transfer are carried out and corroborated using destructive cuts and Energy Dispersive X-ray Spectroscopy (EDX) analysis. The results show that this method can detect internal defects and characterize the material mixing accurately.

# CONTENTS

ACKNOWLEDGMENTS .....	V
ABSTRACT .....	VI
LIST OF ILLUSTRATIONS .....	IX
LIST OF TABLES .....	XIV
NOMENCLATURE.....	XV
Chapter	
I. INTRODUCTION .....	1
II. DISSIMILAR FRICTION WELDING EXPERIMENTS .....	7
A. Material Characterization .....	7
B. FSW Setup .....	8
C. FSW Tools and Parameters.....	9
D. FSW Experiments Results. ....	12
III. NDT CT X-RAY ANALYSIS.....	15
A. CT X-ray Setup.....	15
B. Thresholding and Segmentation Methodology .....	16
C. NDT Analysis of Sample (e).....	19
D. NDT Analysis of Sample (f).....	26
E. NDT Analysis Using Reconstructed Images: .....	31

1. NDT Analysis Using Reconstructed Images of Sample (e).....	32
2. NDT Analysis Using Reconstructed Images of Sample (f) .....	34
<b>IV. SEM/EDX DESTRUCTIVE VERIFICATION .....</b>	<b>37</b>
A. SEM/EDX Setup and Parameters .....	37
B. SEM/EDX Destructive Analysis of Sample (e) .....	39
C. SEM/EDX Destructive Analysis of Sample (f) .....	44
<b>V. DISCUSSIONS AND CONCLUSIONS.....</b>	<b>49</b>
 <b>BIBLIOGRAPHY .....</b>	 <b>55</b>



## ILLUSTRATIONS

Figure		Page
1	FSW setup diagram, key elements are highlighted. ....	8
2	FSW tools tested. (a) cylindrical pin tool with moderate shoulder (12mm). (b) cylindrical pin tool with large shoulder (19mm). (c) conical (tapered) pin tool conducive to better material flow. (d-e) tapered threaded pin tool with circular grooved shoulder the pin shape is considered best for material flow tool (d) and tool (e) have the same shape but with different dimensions. (f) cylindrical tool with a broad shoulder and s small pin used to reduce the generation of internal defects. ....	11
3	Resulting FSW samples from each tool listed in figure 2 respectively. Sample (a) failed weld from too much deformation. Sample (b) bad weld resulting from too much deformation and material overflow. Sample (c), the welds started well but ended with visible defects. Sample (d), the weld shows consistent visible defects across the weld length. Sample (e) showed no visible defects except for a seam line between the two materials. Sample (f) showed no visible defects. ....	13
4	Grey level histogram of the cross-section of weld case #13, the resulting cutoff HU value of 784 is also shown; taken from Hamade and Baydoun [49]. ....	18
5	Segmented cross-section of weld case 13, showing the detected defect to the right; taken from Hamade and Baydoun [49].....	18
6	Photograph of the cross-section of weld sample 13 with the pin-hole defect highlighted in white with a red square marker; taken from Hamade and Baydoun [49].....	19

7	Weld sample (e), (a) photograph of the weld sample, (b) top view of the unsegmented CT image of the weld sample, (d) top view of the CT images of the sample showing in transparent yellow the location of the Otsu thresholding section. ....	20
8	HU histogram for the Otsu thresholding method, calculated thresholds are shown with a vertical red line, mean values for each segment is shown with a vertical blue line and standard deviations in red quotations. ....	22
9	Segmented CT images of sample (e), “Al” and the color red indicated the AA606-T6 alloy, “Mg” and the color blue indicate the AZ31b alloy, (a) top view, (b) cross-sectional view at the section location shown in (a), (c) lateral section across the entire weld length, (d) 3d rendering of the two plates. ....	23
10	Zoomed-in view of cross-section A-A (bottom), the centerline of the weld is marked with a vertical white line. The material mixing is indicated with arrows; the defect area is shown, (top) outline of the tool used for sample (e) shown at the same scale. ....	24
11	3D rendering of the weld sample shown in transparent red and blue, the tunneling defect is shown in solid black with a zoomed-in view to the left. ....	25
12	Weld sample (f), (a) top view photograph of the weld, (b) top view CT image of the weld, (c) top view CT image of the weld sample shown in yellow is the location of the application of the Otsu thresholding.....	26
13	HU level histogram of weld sample (f). The threshold value indicated by a red vertical line, each segment is labeled, the average HU value for each segment is	

	shown in blue and indicated by a blue line, the standard deviation values are shown in brackets. ....	28
14	Segmented CT images of sample (f), “Al” and the color red indicated the AA606-T6 alloy, “Mg” and the color blue indicate the AZ31b alloy, (a) top view, (b) cross-sectional view at the section location shown in (a), (c) lateral section across the entire weld length, (d) 3d rendering of the two plates. ....	29
15	Zoomed-in view of cross-section A-A (bottom) the centerline is shown with a vertical white line, the material mixing is highlighted with arrows, (top) outline of the tool used for sample (f) shown at the same scale. ....	30
16	3D rendering of weld sample (f) the top surface AZ31b material deposit is evident. ....	31
17	HU level histogram of reconstructed images of weld sample (e). the threshold value indicated by a red vertical line, each segment is labeled, the average HU value for each segment is shown in blue and indicated by a blue line, the standard deviation values are shown in brackets.....	32
18	Zoomed-in view of reconstructed cross-section A-A (bottom), the centerline of the weld is marked with a vertical white line. The material mixing is indicated with arrows; the defect area is shown, (top) outline of the tool used for sample (e) shown at the same scale. ....	34
19	HU level histogram of reconstructed CT images of weld sample (f). The threshold value indicated by a red vertical line, each segment is labeled, the average HU value for each segment is shown in blue and indicated by a blue line, the standard deviation values are shown in brackets.....	35

20	Zoomed-in view of the reconstructed cross-section A-A (bottom) the centerline is shown with a vertical white line, the material mixing is highlighted with arrows, (top) outline of the tool used for sample (f) shown at the same scale. ....	36
21	Destructive validation of sample (e). (a) Original cross-section A-A, (b) reconstructed cross-section A-A, (c) SEM images of cross-section A-A overlaid with the EDX point spectrum analysis results. The color bar indicated the percentage of aluminum detected. ....	41
22	Destructive validation of sample (e). (a) Original cross-section A-A, (b) reconstructed cross-section A-A, (c) SEM images of cross-section A-A overlaid with the EDX point spectrum analysis results. The color bar indicated the percentage of magnesium detected.....	42
23	Elemental mapping destructive verification of sample (e). (a) cross-section A-A a yellow rectangle indicates where the mapping analysis was performed. (b) aluminum map, red indicates high aluminum detection. (c) magnesium map, blue indicates high magnesium detection.....	43
24	Destructive validation of sample (f). (a) Original cross-section A-A, (b) reconstructed cross-section A-A, (c) SEM images of cross-section A-A overlaid with the EDX point spectrum analysis results. The color bar indicated the percentage of aluminum detected.....	46
25	Destructive validation of sample (f). (a) Original cross-section A-A, (b) reconstructed cross-section A-A, (c) SEM images of cross-section A-A overlaid with the EDX point spectrum analysis results. The color bar indicated the percentage of magnesium detected.....	47

26	Elemental mapping destructive verification of sample (f). (a) cross-section A-A a yellow rectangle indicates where the mapping analysis was performed. (b) aluminum map, red indicates high aluminum detection. (c) magnesium map, blue indicates high magnesium.....	48
27	Otsu HU histogram of sample (e), transparent black: histogram of the reconstructed cross-sections, solid black: histogram of the original cross-sections. ....	50
28	Otsu HU histogram of sample (f), transparent black: histogram of the reconstructed cross-sections, solid black: histogram of the original cross-sections. ....	51
29	Sample (e), (top) combined EDX elemental analysis of cross-section A-A, (bottom) reconstructed cross-section A-A. ....	52
30	Sample (f), (top) combined EDX elemental analysis of cross-section A-A, (bottom) reconstructed cross-section A-A. ....	54

## TABLES

Table	Page
1 Elemental composition of the AA6061-T6 and AZ31b alloy.....	7
2 FSW parameter ranges used for the 47 FSW experiments. ....	11
3 FSW parameters used for producing the FSW samples shown in figure 3. ....	14
4 CT X-ray scanning parameters.....	15
5 SEM/EDX key parameters.....	38

## NOMENCLATURE

AA6061-T6: An aluminum alloy

AZ31b: A Magnesium alloy

Brilliance iCT 256: X-ray computed tomography machine developed by PHILLIPS

CT X-ray: Computed Tomography X-ray

DICOM: Digital Imaging and Communications in Medicine

EDX: Energy Dispersive X-ray Spectroscopy

FEA: Finite Element Analysis.

FSP: Friction stir Processing

FSW: Friction Stir Welding

HU: Hounsfield Unit

INCA: Energy dispersive X-ray spectroscopy software developed by OXFORD

Instruments

MATLAB: A computing software and programming language developed by

MATWORKS

MIMICS: Image processing software developed by MATERIALISE

MIRA3: Scanning electron microscope and accompanying software developed by

TESCAN.

NDE: Non-destructive Evaluation

NDT: Non-destructive Testing

RPM: Rounds Per Minute

SEM: Scanning Electron Microscope

TAZ: Thermally Affected Zone

TMAZ: Thermally and Mechanically Affect Zone

# CHAPTER I

## INTRODUCTION

The quality assurance of a manufactured product has been implemented in all types of factories and plants. Recently nondestructive evaluation and testing methods (NDE and NDT) have seen increasing popularity in the manufacturing sector especially in the evaluation of critical components such as stringers, turbine blades, engine blocks, and critical welds [1-4].

For example, Petit et al. [5] used X-ray tomography to study the effect of intermetallic compounds on the mechanical properties of aluminum foam samples and were able to confirm via finite element analysis (FEA) that the presence of these compounds results in failure of these foams. Moura et al. [6] successfully employed gamma-ray CT to analyze welded steel tubes for discontinuity in the weld zone recoding discontinuities as small as 0.3mm.

Plessis and Rossouw [7] used X-ray micro CT in order to detect defects and study the wall thickness consistency of an aerospace part made from titanium by investment casting. Plessis and Rossouw[7] were able to detect defects with volumes as low as  $2\text{mm}^3$ . Zheng et al. [8] employed two NDT methods for the detection of voids, determining volume fraction, and analyzing the shape of the adhesive fill. The first method was neutron radiography and was used to determine the void fraction by thresholding the neutron radiography images and to calculate the ratio of void pixels to material pixels. X-ray CT



allowed for clear visualization of the defects due to the high resolution of the scans of 125  $\mu\text{m}^3$  [8]. Hermanek and Carmignato [9] used an aluminum object to which different void like features were added in order to determine the effectiveness of X-ray CT scans in detecting these features accurately, a total of 72 machined features were added to the object. The representational accuracy of the scans was studied and evaluated based on multiple criteria and based on comparisons with numerical simulations [9].

Friction stir welding (FSW) is a welding technique credited to T.W Morris. This method involves pressing a welding tool that does not remove material into the workpiece plates and then traversing the weld length while the tool rotates at high speeds, thus causes significant shearing action or stirring which welds the plates together [10]. Developed in 1992, one of the notable advantages of this welding method is that it applies to a multitude of materials such as steel, aluminum, magnesium, titanium, among many [11-14]. FSW can be used to weld these metals to themselves (same material weld) or to other (dissimilar material welds) [15-18].

The aluminum alloy AA6061-T6 and the magnesium alloy AZ31b are relatively new alloys that present high strength to weight ratios, as well as other attractive qualities such as recyclability and ease of machining. These properties made these alloys highly sought-after materials in numerous industrial fields, especially in automotive and aerospace where light materials result in increased efficiency and profitability [19-25].

These two alloys are well studied in FSW. For example, Hilal et al. [26] performed FSW lap welds on AA6061-T6 and ultra-low carbon steel and studied the effects of the feed speed on intermetallic compound formation, the weld zones (TMAZ and HAZ ) and

generated shear loads. Elangovan and Balasubramanian [27] studied the effect of post welding heat treatment on the tensile properties of FSW AA6061 joint. Their findings show that simple artificial aging increases joint efficiency by 11%. Fathi et al. [28] performed underwater FSW of AA6061, by lowering the welding temperature Fathi et al. [28] were able to prevent the HAZ from softening and thus improving the weld strength and hardness by 16% and 12.5% respectively.

Xu et al. [29] investigated the effects of extremely low welding speed, and rotational tool speed on the microstructure of FSW butt welded AZ31b plates. The extremely low welding parameters resulted in a twin structure in the weld zone which acts as a barrier to dislocation movement and thus improving mechanical properties. Han et al. [30] employed electrically assisted friction stir welding to join AZ31b plates with a current range of 0 to 200A and studied the current effect on the tensile strength of the joints. Han et al. [30] noted that with increased current a higher tensile strength was achieved reaching a weld effectiveness of 84.95% of the base metal at 200A. Gulati et al. [31] produced FSW joint of AZ31b using two tools with different pin geometries (cylindrical and conical), visual inspections of the welds were made, and the optimal FSW for each pin geometry was determined.

Meng et al. [32] studied the improvement resulted from using an ultrasonic generator to reduce the material adhesion on the pin of the FSW tool for dissimilar AA6061-T6 and AZ31b dissimilar FSW butt welds. Using this method, the welded joint reached a tensile strength of 115MPa. Sharma et al. [33] performed dissimilar FSW experiments on AZ31b and AA6061 circular plates; five different tools were tested.

Sharma et al. [33] noted that the circular geometry poses more difficulty during welding compared to linear welds. A Cylindrical pin geometry, and a rotational speed of 1200RPM and feed of 10mm/min were found to produce the best welds [33]. Mehta et al. [34] investigated conventional and cool assisted FSW of dissimilar AA6061 and AZ31b alloys, the welds were analyzed using EDX, X-ray diffraction, tensile testing, and microhardness indentation. Cooled FSW showed improved tensile strength and hardness over conventional FSW, and improved weld efficiency of 20% [34].

The application of NDT methods towards the evaluation of FSW joints has been an important area of research in recent years, multiple testing techniques have been implemented to determine the quality of an FSW joint. They generally focus on the detection of internal defects since the presence of these defects will drastically lower the strength of the weld. Common defects encountered in metal friction stir welding include chip defects, wormhole defects and scalloping defects, each of these defects is characterized by a specific geometry [35 36].

One example of such studies is the usage of ultrasonic waves that react to the change in density that corresponds to the presence of a defect. Tabatabaeipour et al. [37 38] demonstrated that ultrasonic waves could be used to study the root defects in butt-welded FSW joints. Lamb waves were also successfully employed by Santos and Santos [39] to detect internal defects in butt-welded aluminum plates. As noted by Santos and Santos [39], however, X-rays can be employed in relatively the same way as ultrasonic waves and will give more quantitative details about the defects. Schaff et al. [40] developed a method based on X-ray CT to study FSW aluminum alloy samples; this

method allowed for higher resolution than traditional CT X-ray methods. Maho et al. [41] manufactured dissimilar Al-Steel FSW welds using an underwater technique to reduce heat generation and therefore, the formation of intermetallic compounds. Welds were then analyzed using micro X-ray CT to detect the presence of kissing, cavity and “lazy S” defects in the weld zone. Dumont et al. [42] analyzed FSW AA7449 joints using small-angle X-ray scattering and were able to reveal the microstructure of the weld as well as the different weld zones. Egan et al. [43] developed an “instrument with the ability to spatially resolve energy-dispersed X-ray powder diffraction patterns taken in a single snapshot.” Bead on plate FSW Al7050-T6 was used to test the accuracy of the developed instrument. The instrument detected the different crystalline phase in the weld zone.

The evaluation of material mixing is, however, a more laborious task since the test or evaluation technique must be able to detect the changes in physical properties of the materials such as radiodensity for X-ray based techniques. In X-ray based defect detection NDT techniques, the radiodensity between air (internal voids) and metals is significant, allowing for relatively straightforward detection of defects. However, since the radiodensity changes between metals are generally less pronounced than the radiodensity changes between these metals and air, applying X-ray NDT methods towards the analysis of material mixing is a more challenging task.

Schneider et al. [44] employed an X-rays and X-ray CT scans to determine the mixing of material in aluminum FSW, to overcome the radiodensity problem mentioned above, Schneider used a lead wire to act as a tracker element. The tracker element was then used to study the effect of tool rotation, and shearing action, that is then used to

evaluate the structure of the weld. Morisada et al. [45] employed a similar technique but using tungsten as the tracer element, 3D plots corresponding to the tungsten flow were plotted.

The previous studies, while offering new insight into material flow evaluation, lacked critical elements regarding the X-ray implementation and methodology. The thresholding methodology that allows for the segmentation of the masks is not adequately described. This methodology is critical since using an accurate thresholding method would allow for a more in-depth analysis of material flow analysis and internal defects size determination. Applying such a methodology will offer multiple new quantitative elements that can be analyzed and studied to optimize weld parameters and obtain stronger welds.

In this research, a method for material flow analysis and defect detection by based on computed tomography X-ray (CT X-ray) scans is presented, tested, and corroborated. First dissimilar friction welded AA6061T6/AZ31b welds are produced. The welded samples are then analyzed using the proposed NDT CT X-ray method. Based on the Hounsfield Units scale (HU) [46 47], the CT X-ray scans are segmented using the global Otsu thresholding method [48] into masks for each different material, and 3D renderings are generated. Measurements of materials penetration and transfer are carried out and corroborated using destructive cuts and Energy Dispersive X-ray Spectroscopy (EDX) analysis.

## CHAPTER II

### DISSIMILAR FRICTION WELDING EXPERIMENTS

In this chapter, the characteristics for the material used is presented, and the methodology used to produce the dissimilar friction stir welds is outlined. The resulting welds are then presented

#### A. Material Characterization

The materials to be used in this research are AA6061-T6 and AZ31b. The composition of which was obtained via Energy Dispersive X-ray Spectroscopy (EDX) and is listed in table 1. These materials were selected because they are relatively easy to weld (lower welding forces is required compared to low carbon steel) and are well researched [26-34] also because of previous FSW experience with these materials [49-51]. Furthermore, these -materials exhibit a measurable difference in their radioactive response when subjected to CT X-ray; thus, it is possible to efficiently differentiate the two materials in a CT X-ray image.

Table 1 Elemental composition of the AA6061-T6 and AZ31b alloy.

% Weight	Al	Mg	Zn	Fe	Si	Cu	Mn
AA 6061-T6	98.51	0.88	0.44	0.03	0.03	0.1	ND
AZ31b	2.52	96.38	0.79	ND	ND	ND	0.31

## B. FSW Setup

The welding was performed using a HAAS VF-6 5-axis milling center, to which a prebuilt FSW fixture is attached to enable welding. The plates are FSW'ed in a butt weld configuration. Figure 1 shows the FSW setup with the essential elements labeled, the FSW fixture (3) is placed in the KURT vice (2). The FSW Tool (4) is placed in the spindle (1) and the position calibrated to dimensions of the plates and the weld start position. The plates (5-6) are secured via the clamping mechanism (7-9). Dry compressed shop air (10) is used to cool the tool during and after each weld.

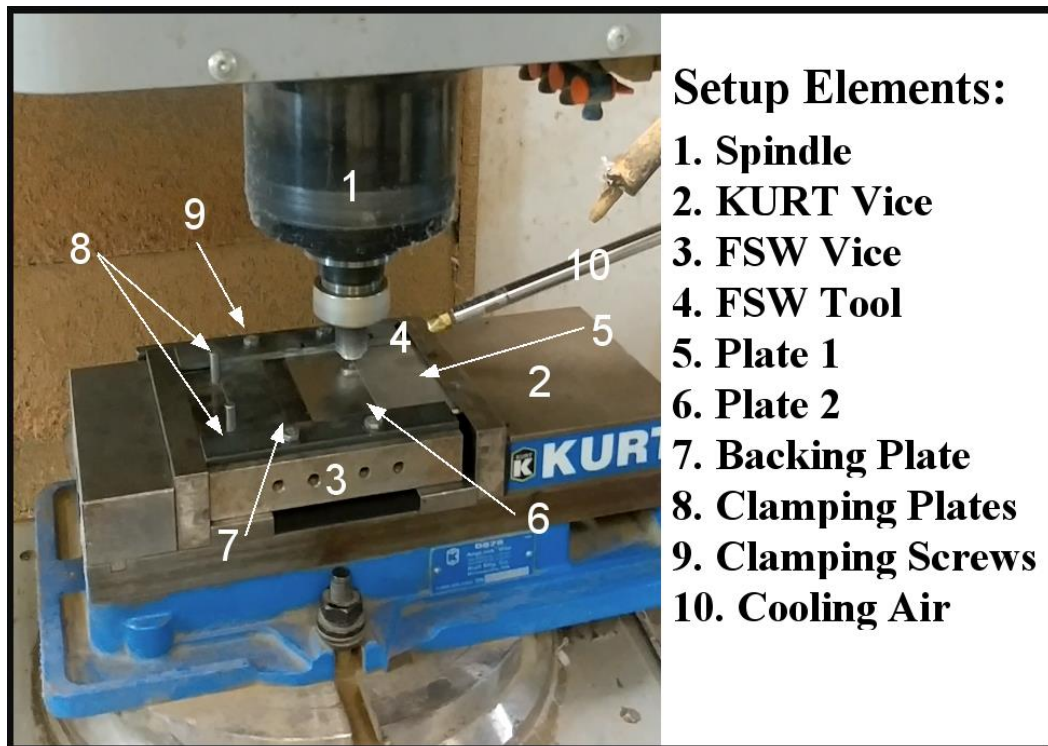


Figure 1 FSW setup diagram, key elements are highlighted.

### C. FSW Tools and Parameters

A total of 6 tools were tested at multiple feed/speed/offset combinations in order to determine the optimal tool for dissimilar AA6061-T6/AZ31b FSW. Traditional FSW tools having cylindrical pins and simple shoulders were tested, a conical tool and two threaded pin tools with circular shoulder grooves. Due to the highly non-linear coupled physical phenomena encountered in FSW [18] selecting the proper tool for a particular weld configuration is an involved task and the reason why multiple tools were tested.

Figure 2 (a-f) show the tools used, tool (a) is a traditional FSW tool with a 6mm diameter pin and 12 mm diameter shoulder. Tool (b) is also a traditional FSW tool but with a broader shoulder to increase the welding area. Tool (c) has a cone-shaped pin, note that this tool geometry facilitates material flow. Tools (d) and (e) are threaded cone-shaped tools with a grooved shoulder that generally results in the highest strength welds due to the material flow patterns that are observed during welding the main difference between these two tools are the dimensions of the pin and shoulder features. Tool (f) is a traditional cylindrical tool with a small pin (3mm) and a large shoulder (21mm) that results in sufficient material flow without introducing too much deformation into the weld zone [52-55].

A total of 47 welds were produced, the feed, speed, and tool offset ranges are listed in table 2. The weld length of all welds was 57mm measured from the start position to the center of the exit hole of the welds. For each tool, a few initial tests were conducted at different parameter combination based on previous FSW experiments. These welds were then evaluated and used as a base point for the following tests. For the first two tools (a



and b) however, a total of four welds were used, and it was concluded early on that the pin geometry was too large and the resulting shearing action was too violent on the material meaning that no significant welding is viable.

The tools showed variable performance depending on the parameter combinations used. The samples were visually inspected after welding. The presence of visible defects was used as a measure for the selection of the next FSW parameters. While the absence of visible defects is not a measure of the strength of the weld due to the possible presence of internal non-visible defects, it is a suitable parameter in this case since the objective is to produce both good welds as well as welds that contain internal defects to be detected by the NDT method.

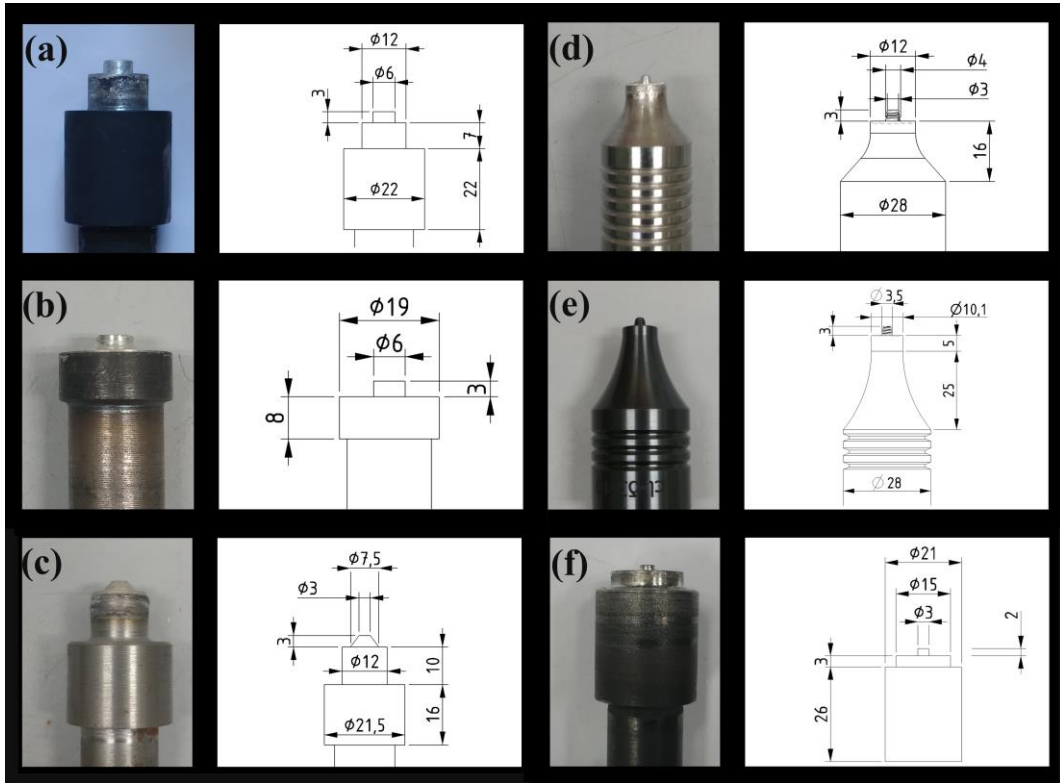


Figure 2 FSW tools tested. (a) cylindrical pin tool with moderate shoulder (12mm). (b) cylindrical pin tool with large shoulder (19mm). (c) conical (tapered) pin tool conducive to better material flow. (d-e) tapered threaded pin tool with circular grooved shoulder the pin shape is considered best for material flow tool (d) and tool (e) have the same shape but with different dimensions. (f) cylindrical tool with a broad shoulder and a small pin used to reduce the generation of internal defects.

Table 2 FSW parameter ranges used for the 47 FSW experiments.

Parameter	Range
Speed	900-3000 RPM
Feed	25-600mm/min
Offset	±2mm ( depending on tool pin diameter)

#### **D. FSW Experiments Results.**

Figure 3 shows a selection of the best samples produced by each tool; the FSW parameters used to produce each weld are presented in table 3. Each sample is numbered after the respective tool used in the FSW operation. Tool (a), as previously stated resulted in excess material shearing at a high rate so that the material was pushed away by the large pin, no mixing took place this can be clearly seen in figure 3 (a). Tool (b) showed similar behavior as well resulting in a similar result to tool (a) figure 3 (b). Sample (c) started with good weld and good surface finish. However, a large groove formed in the end half of the weld. Sample (d) showed a consistent rate of visible defects across the weld length. Sample (e) showed good surface finish across the weld length, and no visible defects were observed in the weld except for a seam line at the interface between the two metals. Sample (f) also showed good surface finish. No visible defects were observed for that sample.

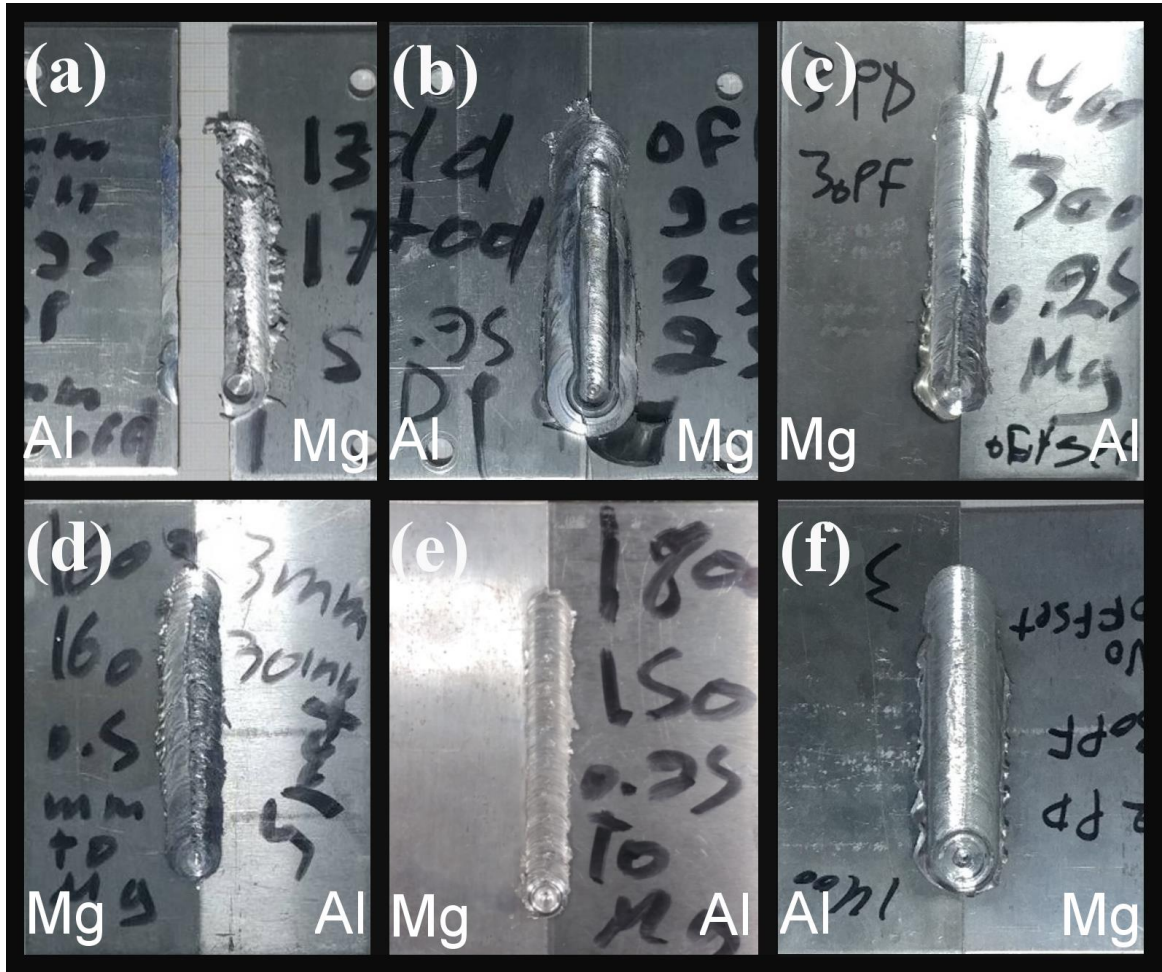


Figure 3 Resulting FSW samples from each tool listed in figure 2 respectively. Sample (a) failed weld from too much deformation. Sample (b) bad weld resulting from too much deformation and material overflow. Sample (c), the welds started well but ended with visible defects. Sample (d), the weld shows consistent visible defects across the weld length. Sample (e) showed no visible defects except for a seam line between the two materials. Sample (f) showed no visible defects.

Table 3 FSW parameters used for producing the FSW samples shown in figure 3.

Sample	Parameters					
	Speed (RPM)	Feed (mm/min)	Plunge depth (mm)	Offset (mm)	Advancing	retracting
a	1300	175	3	2 to AZ31b	AZ31b	AA6061-T6
b	900	25	3	0	AZ31b	AA6061-T6
c	1400	300	3	0.25 to AZ31b	AA6061-T6	AZ31b
d	1600	160	3	0.5 to AZ31b	AA6061-T6	AZ31b
e	1800	150	3	0.25 to AZ31b	AA6061-T6	AZ31b
f	1400	300	2	0	AZ31b	AA6061-T6

These results show that as expected the threaded pin tool does indeed result in good material flow and therefore proper mixing, however, this does depend on the dimensions on the features since better results were obtained using tool (e) than tool (f). It was also found that a tool with a small pin would also result in a good weld given the optimal FSW parameters are used.

These experiments showed that for the tools used the ideal speed range is 1300-1800 RPM, the ideal feed range is 150-300 mm/min, and that an offset into the softer material (AZ31B) further improves the weld quality as well. Samples (e) and (f) are selected for the CT X-ray NDT analysis since they show good weld characteristics, and no surface defects were observed in the weld.

## Chapter III

### NDT CT X-ray Analysis

#### A. CT X-ray Setup

The X-ray CT scans are performed using a Philips/iCT 256 CT machine, at a 16-bit depth such that the sample is placed on a leveled table supported only at the corners such that the weld is in direct contact with air and not any other material. The scanning is conducted in the direction of the z-axis of the scanning machine. The CT X-ray machine parameters are presented in table 4. The CT data (DICOM images) is analyzed using the software MIMICS Research (MATERIALISE).

Table 4 CT X-ray scanning parameters.

Parameter	value
Voltage	120KV
Tube Current	293mA
Slice thickness	0.67mm
Slice Spacing	0.335mm
Field of View	125mm

## **B. Thresholding and Segmentation Methodology**

In order to characterize the mixing and detect internal defects in the weld zone, it is necessary to segment the raw DICOM images into regions corresponding to each material exclusively. In this work, this is accomplished by utilizing the HU scale [46-47] and the Otsu thresholding method [48].

The HU scale was developed in 1977 by R.A. Brooks. The unit is based on the X-ray attenuation coefficient and normalized with respect to the X-ray attenuation of water and air. The HU value of water is zero, and that of air is -1000 HU [46]. Different materials will have different HU values depending on the radioactive properties as well as the X-ray machine parameters, mainly the voltage and tube current [56]. Depending on the alloying (elemental composition) as well as the sample geometry and CT X-ray parameters different values were reported for aluminum ranging between 1800 to 2329 [56-59]. However, since the CT X-ray scans include some averaging when transitioning from the material to another as well as noise and saturation, a method is needed to divide the CT X-ray images into sections corresponding to each material separately while mitigating those problems.

In this research this is done by utilizing the Otsu thresholding technique which is based on the gray level histogram of the image and the probability of occurrence of each group of pixels (foreground and background) for a given threshold, selecting the optimal threshold that maximizes the between-groups variance. Based on the number of regions wanted, one or multiple thresholds can be determined using this method [48]. The

implementation is accomplished in MATLAB using the “Multithresh” built-in command, the command uses the Otsu thresholding method and thus is well suited for this task.

In Hamade and Baydoun [49] the author has previously demonstrated that the Otsu thresholding method can be successfully employed to detect defects in dissimilar FSW lap joints. By applying the Otsu method on a weld cross-section presenting the gray level histogram shown in figure 4 is obtained, also shown in figure 4 is the Otsu threshold value of 784 HU which intermediate to the HU of defects (-1000) and that of Al (1800-2300). The graph showed the expected bimodal shape that is indicative of a background/foreground mode, which in this case corresponds to a material/defect combination. However, because the defect was small, and the pixel resolution low the shape of the defect was not captured accurately [49]. The resulting CT X-ray cross-section is shown in figure 5, and the material mask is shown in light blue. A defect with a size of 8 pixels is detected based on the applied thresholding scheme. This was verified by destructive cutting of the sample at the same cross-section, which showed a pin-hole defect that the expected location as can be shown in figure 6 which is a photograph of the cross-section. The defect is highlighted in white and a marked with the red square.



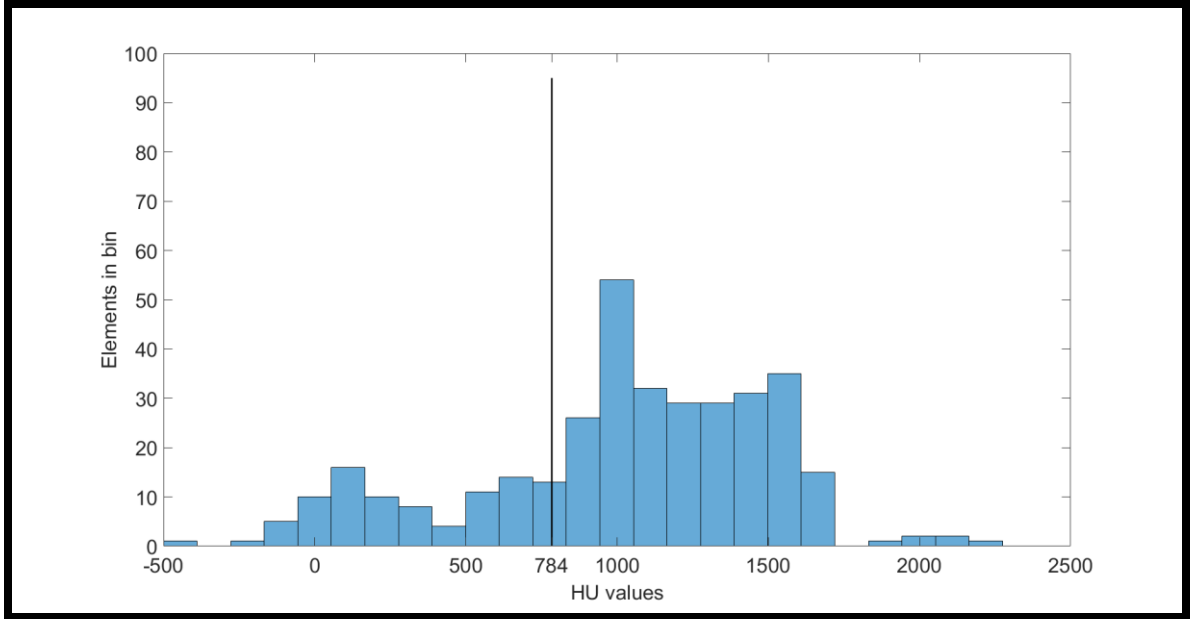


Figure 4: Grey level histogram of the cross-section of weld case #13, the resulting cutoff HU value of 784 is also shown; taken from Hamade and Baydoun [49].



Figure 5 Segmented cross-section of weld case 13, showing the detected defect to the right; taken from Hamade and Baydoun [49].



Figure 6 Photograph of the cross-section of weld sample 13 with the pin-hole defect highlighted in white with a red square marker; taken from Hamade and Baydoun [49].

This methodology is adjusted by utilizing the multiple segment Otsu thresholding in order to create three segments instead of two since as well as detecting defects, the analysis of mixing between the two different aluminum and magnesium alloy is wanted as well. Thus, obtaining a segment of air, AZ31b, and AA606-T6 alloys. In this research, this is accomplished by applying the thresholding method on all cross-sections of the weld for the entire weld length as to obtain average thresholds that can be applied to any cross-section individually and give accurate results.

### **C. NDT Analysis of Sample (e)**

This analysis is first applied to sample (e). The sample is first scanned by the CT X-ray machine, as described in section A of this chapter. Figure 7 (a) shows a top view photograph of the weld sample as well as a CT image (b) shown from the same perspective. By examining the CT X-ray image, it can be noted that the difference between the two alloys AZ31b and AA6061-T6 can already be noted with the AZ31b plate

appearing in a darker gray than the AA6061-T6 plate, this indicates a difference in the HU values of these alloys. The Otsu thresholding method is applied across all the weld length as above mentioned, figure 7 (c) shows in yellow the location where the thresholding was applied.

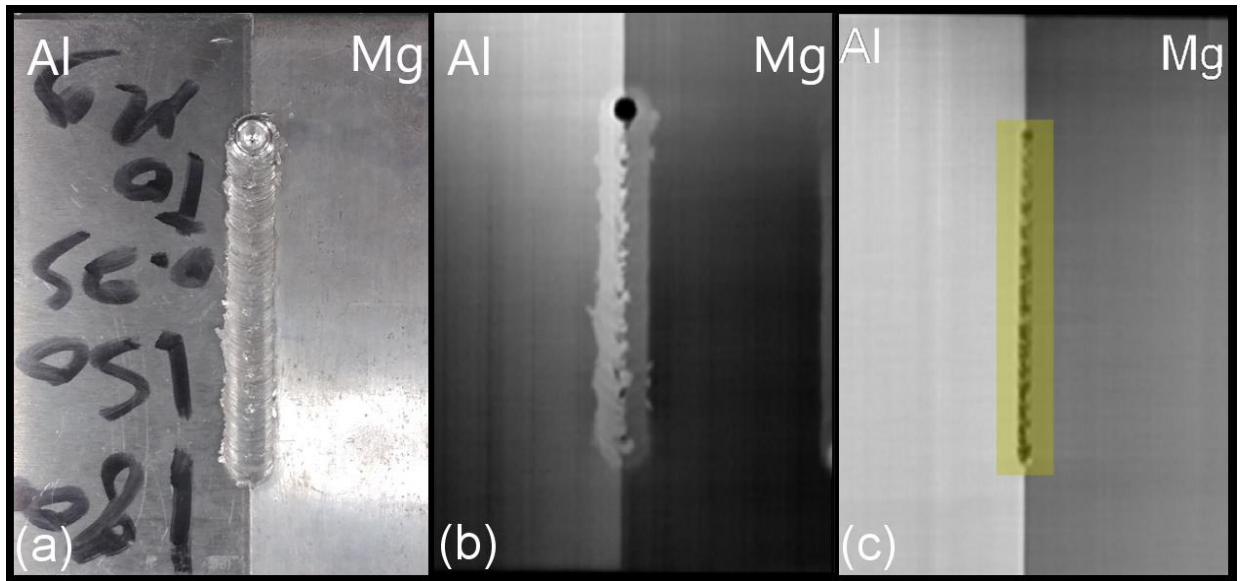


Figure 7 Weld sample (e), (a) photograph of the weld sample, (b) top view of the unsegmented CT image of the weld sample, (d) top view of the CT images of the sample showing in transparent yellow the location of the Otsu thresholding section.

The resulting histogram is shown in figure 8. The histogram has the ideal trimodal distribution corresponding to the three materials present AA6061-T6 AZ31b and air (defects and voids), thus making the histogram segmentation reliable and accurate. The threshold values are shown on the X-axis and segment the histogram via a vertical red lines; the reliability measure of this segmentation is 0.918. The two thresholds are 56 HU and 1162 HU. For each segment the mean HU value is calculated (shown with a blue line) as well as the standard deviations (shown in red quotations). The mean HU value of AA6061-T6 is 1727 HU which is around the expected theoretical range, separated by

around 1100 HU from the mean HU value of the AZ31b at 602 HU. The internal defects (voids) show a mean HU value of -481HU the negative value indicate that it corresponds to air, but due to the averaging process with nearby material pixel this value is shifted from the theoretical -1000 HU value. For the magnesium (AZ31b) region the majority of the elements are within one standard deviation of the average value in a symmetrical manner, however, for the aluminum (AA6061-T6) region the peak shows a clear trailing edge with a secondary peak at 1920 HU. For the defect region, the standard deviation is significant due to the shape of the region, the main peak for the defect region is at -1000 HU which shows a sharp decrease -850 HU, at this value the decrease in bin elements is halted until around 700 HU where the bin elements start to gradually increase again. The defect region exhibit an inverse bell-shaped distribution with a pronounce peak the left-most side and a slight peak at the right-most side, this is due to the fact that the ideal value for defect region at an extremely high-resolution scan with no averaging phenomenon is -1000HU, but since the averaging process is still observed at the valley between the peaks of the defect and material segment still shows a consistent number of elements. The aim of employing the Otsu thresholding is to separate these elements into the different material segment in the best way as to preserve the accuracy of any measurements taken from these CT images.

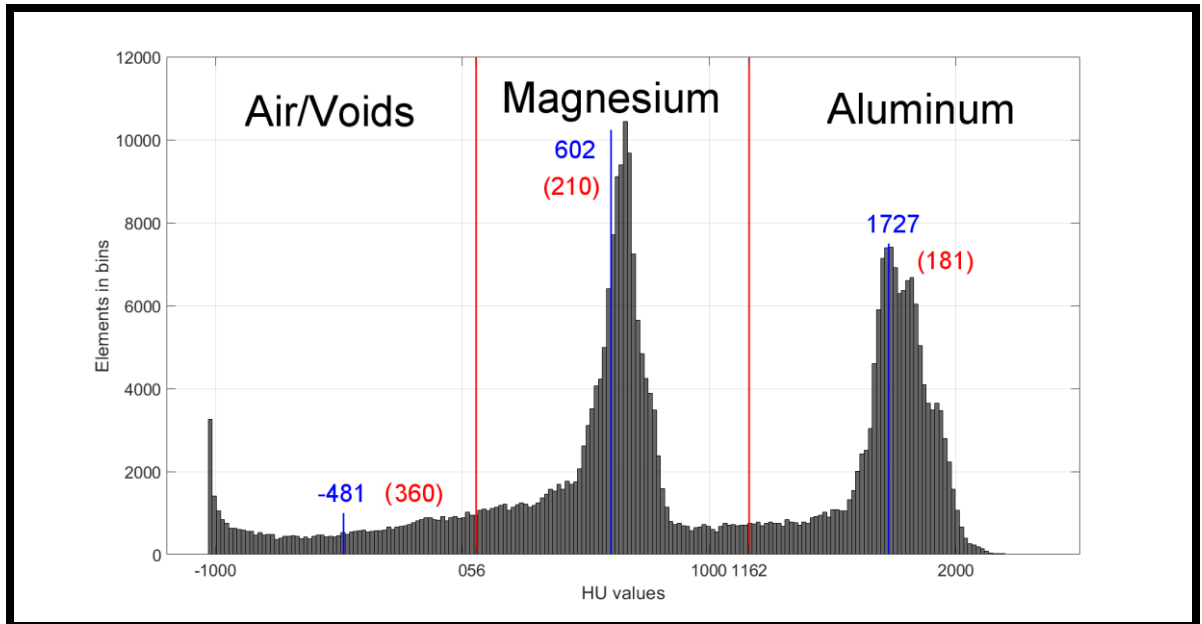


Figure 8 HU histogram for the Otsu thresholding method, calculated thresholds are shown with a vertical red line, mean values for each segment is shown with a vertical blue line and standard deviations in red quotations.

Figure 9 shows three segmented projection view of sample (e) the “Al” symbol and the color red indicated the AA6061-T6 alloy and the “Mg” symbol and the blue color indicate the AZ31b alloy. Figure 9 (a) shows the top view of the weld sample with the location of a section showing interesting mixing patterns indicated by the section arrows A-A. This section shown in figure 9 (b) shows a large tunneling defect as well as AA6061-T6 penetration into the AZ31b plate at the top and bottom of the weld cross-section, as well as some AZ31b into the AA6061-T6 at mid-section. Figure 9 (c) shows the lateral section of the weld length, indicating that the tunneling defect observed in section A-A is also present across the entire weld length. Using the 2D masks created using the applied thresholding method, a 3D rendering of the two plates was also created; this is shown in figure 9 (d).

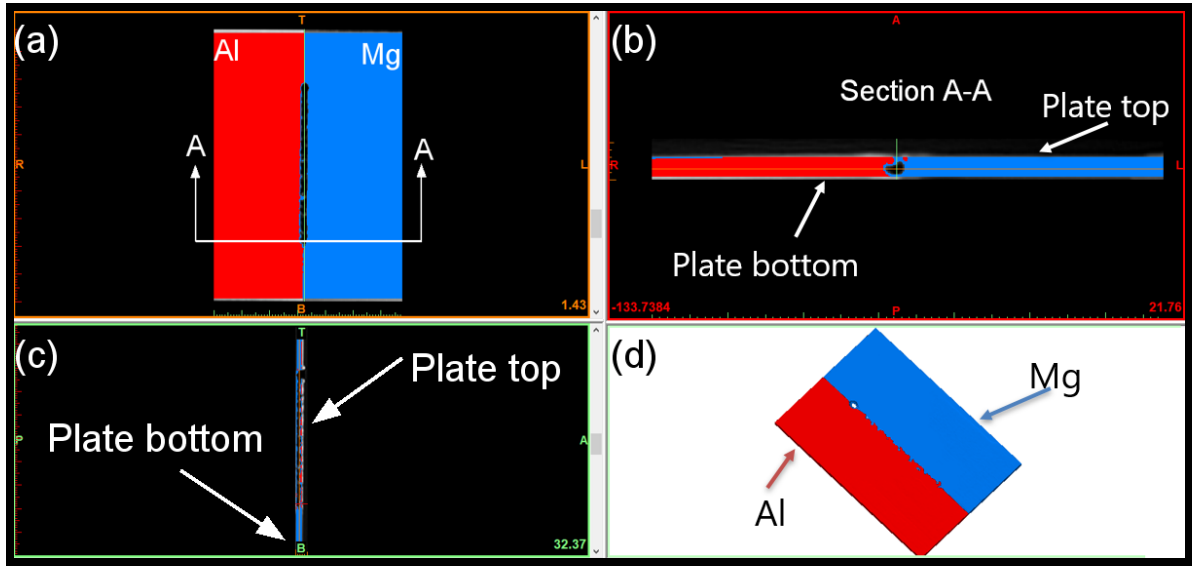


Figure 9 Segmented CT images of sample (e), “Al” and the color red indicated the AA606-T6 alloy, “Mg” and the color blue indicate the AZ31b alloy, (a) top view, (b) cross-sectional view at the section location shown in (a), (c) lateral section across the entire weld length, (d) 3d rendering of the two plates.

Figure 10 shows a zoomed-in view of cross-section A-A of sample (e) on top of which the tool outline is shown using the same scale as the cross-section. In this figure, the AA6061-T6 material penetration is more evident mainly the AA6061-T6 deposit at the top of the weld that is separated from the main plate body of the AA6061-T6 alloy indicating that the threaded pin resulted in a depositing/mixing action that is atypical of this pin geometry. There is some AA6061-T6 penetration that is detected on the bottom of the plate as well while the primary AZ31b penetration into the AA6061-T6 is mainly detected at the middle of the cross-section. As for the tunneling defect the cross-sectional area of the defect is measured as  $2.63\text{mm}^2$ . The tunnel is further indication of atypical mixing action taking place. Ideally internal defects would be much smaller, this weld, however, can still be used as an example of this method’s ability to evaluate and defects.

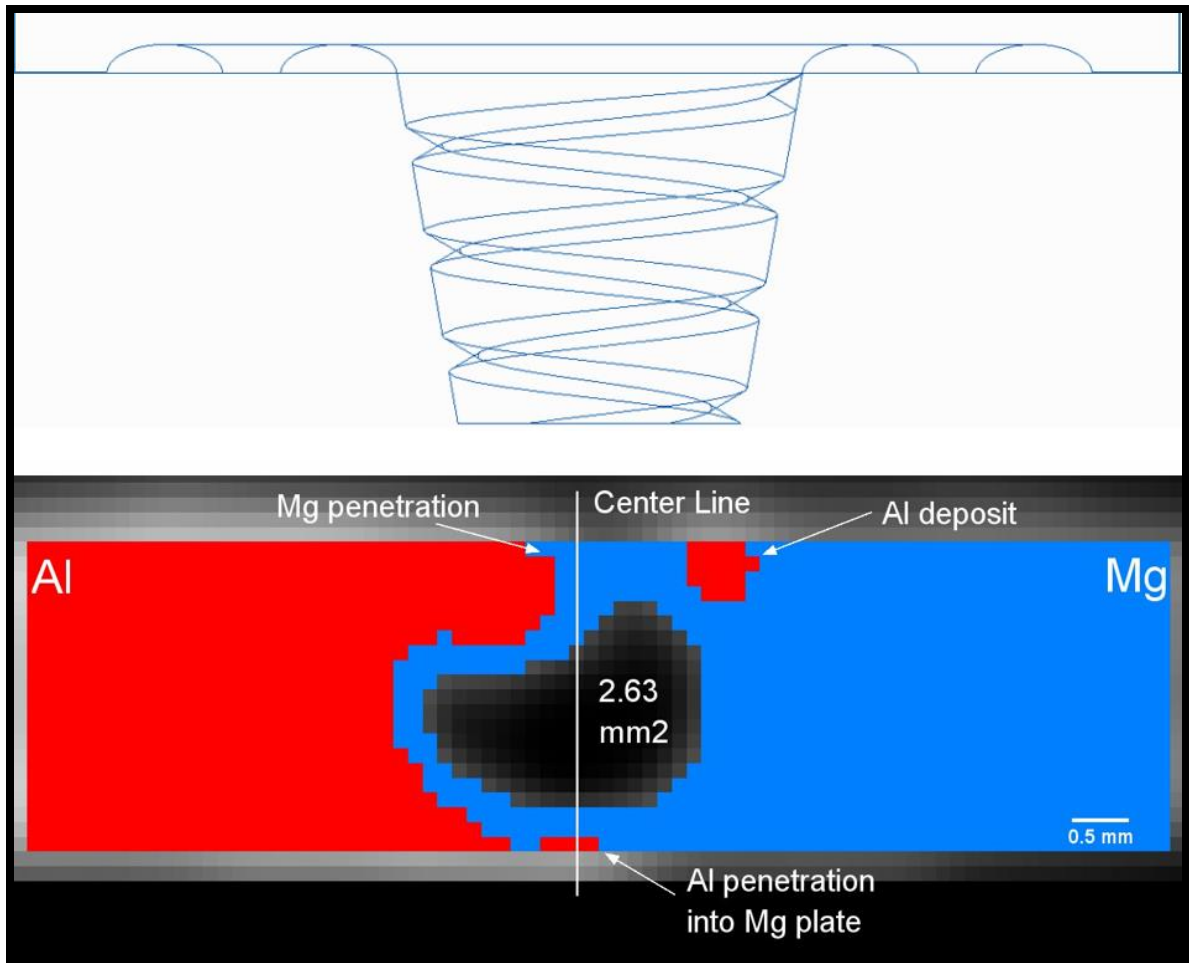


Figure 10 Zoomed-in view of cross-section A-A (bottom), the centerline of the weld is marked with a vertical white line. The material mixing is indicated with arrows; the defect area is shown, (top) outline of the tool used for sample (e) shown at the same scale.

To measure the volume of the detected tunneling defect, a 3D object was constructed for the internal defects as well. Figure 11 shows this 3D reconstruction, the AA6061-T6 and AZ31b plates are shown in transparent red and blue respectively, the tunneling defect is shown in solid black, 3D volume measurements show that the tunneling volume is  $180\text{mm}^3$  with the exit hole and  $164\text{mm}^3$  excluding the exit hole. Alternatively, the defect volume can be calculated based on the number of pixels in the void mask, the tunnel mask contained a total of 32386 elements, with a voxel size of  $0.00566\text{mm}^3$  this

leads to a tunnel volume of  $183\text{mm}^3$ , this is a volume increase of 1.6%. The NDT of the tunneling defect highlights the need and importance of the NDT and NDE of FSW joints since after the NDT analysis was carried out the quantitative data (volume and cross-sectional area) were calculated, allowing for a deeper understanding of the effect of pin geometry and FSW parameters on the generation of internal defects.

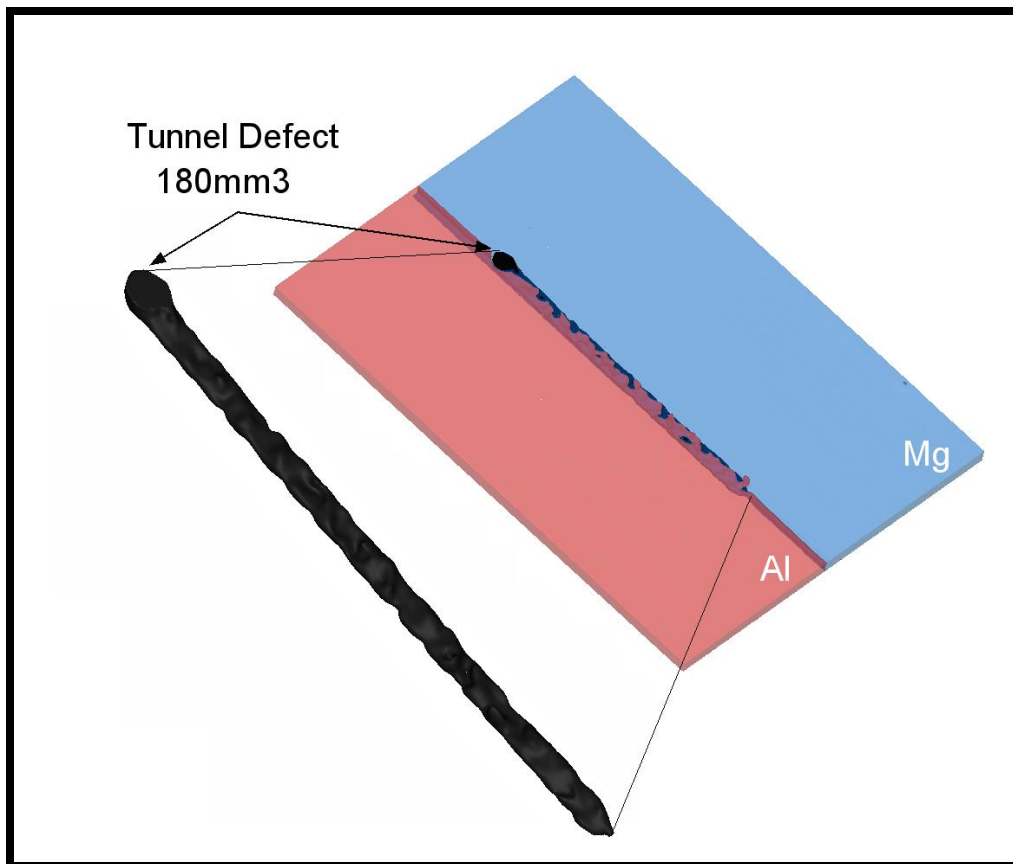


Figure 11 3D rendering of the weld sample shown in transparent red and blue, the tunneling defect is shown in solid black with a zoomed-in view to the left.



#### D. NDT Analysis of Sample (f)

The NDT method is applied to weld sample (f); the same methodology is adopted. Figure 12 (a) shows a photograph of the weld sample, figure 12 (b) shows the non-segmented CT image of the weld sample, again it can be noted that the AA6061-T6 plate appears in a lighter shade of gray than the AZ31b alloy plate. Figure 12 (c) shows in yellow the location where the Otsu thresholding was applied, which is the entire weld length. The sample showed the best surface finish of the other weld samples.

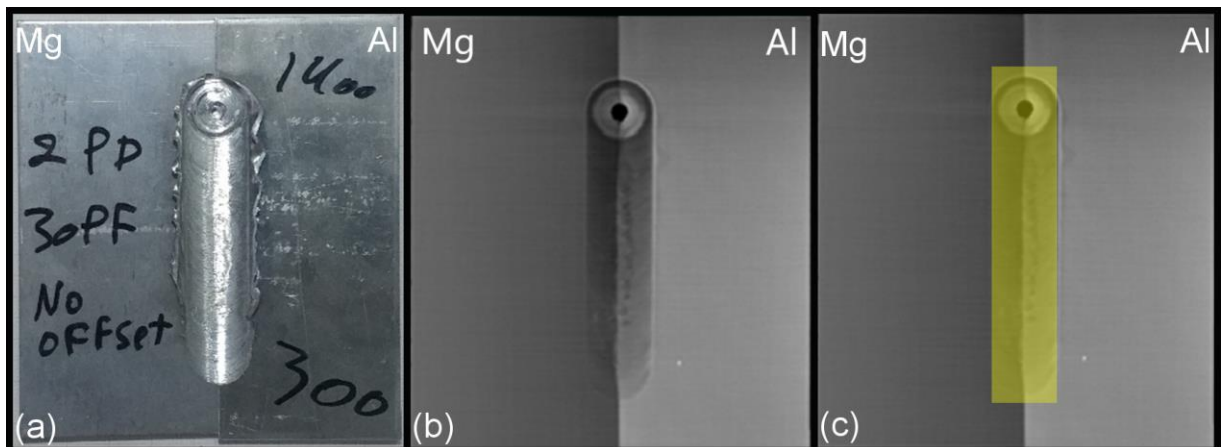


Figure 12 Weld sample (f), (a) top view photograph of the weld, (b) top view CT image of the weld, (c) top view CT image of the weld sample shown in yellow is the location of the application of the Otsu thresholding

The HU level histogram for sample (f) is shown in figure 13, in this case also a trimodal distribution is observed, however the peak at the -1000 HU value is significantly smaller than the peaks at 483 HU (AZ31b peak) and 1689 HU (AA6061-T6 peak). This is indicative of the absence of internal defects, the small peak that is shown is related to the exit hole of the weld more evident when comparing with the HU histogram of sample (e) the elements in bins -250 to -1000 is significantly reduced further confirming the absence

of defects. The recorded HU mean values for both alloys is 483 HU and 1689 HU respectively for AZ31b and AA6061-T6. Since no defects were detected the threshold between the AZ31b and air (voids/ defects) is not needed. The histogram also shows secondary peaks next to the right of both peaks; this is indicative of proper mixing because the interface pixels (pixels located at the interface between the two materials) will have HU values that are intermediate to the HU values of both alloys taken separately. This is not observed in the HU histogram of sample (e) due to the presence of the tunneling defect. Both alloys have an extensive interface with air (defects) and thus the change in HU occurs mostly from the materials mean HU value to -1000 at a fast pace due to the high pixel resolution of the scan and the broad range between the two mean values especially when compared to the range between the mean HU values of both alloys. The Otsu thresholding for sample (f) resulted in a threshold value of 1082 HU, with a reliability measure of 0.871.

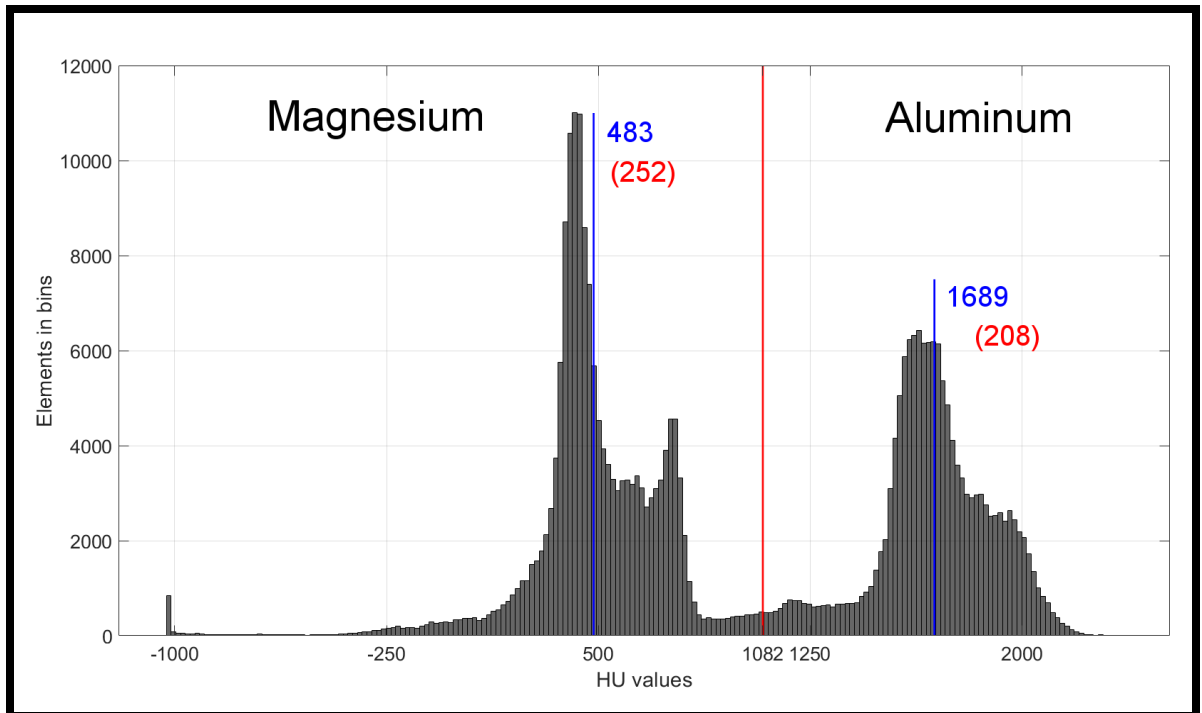


Figure 13 HU level histogram of weld sample (f). The threshold value indicated by a red vertical line, each segment is labeled, the average HU value for each segment is shown in blue and indicated by a blue line, the standard deviation values are shown in brackets.

The segmented images are shown in figure 14, the same color scheme and labeling as the above section are used here. Figure 14 (a) shows the top view of the segmented sample; the section arrows indicate a cross-section selected for further analysis. Figure 14 (c) shows the lateral section across the weld length. Figure 14 (d) shows the 3D rendering generated from the 2D masks. Figure 14 (d) shows that for this weld at the weld top surface, a large amount of AZ31b was transferred to the AA6061-T6 plate.

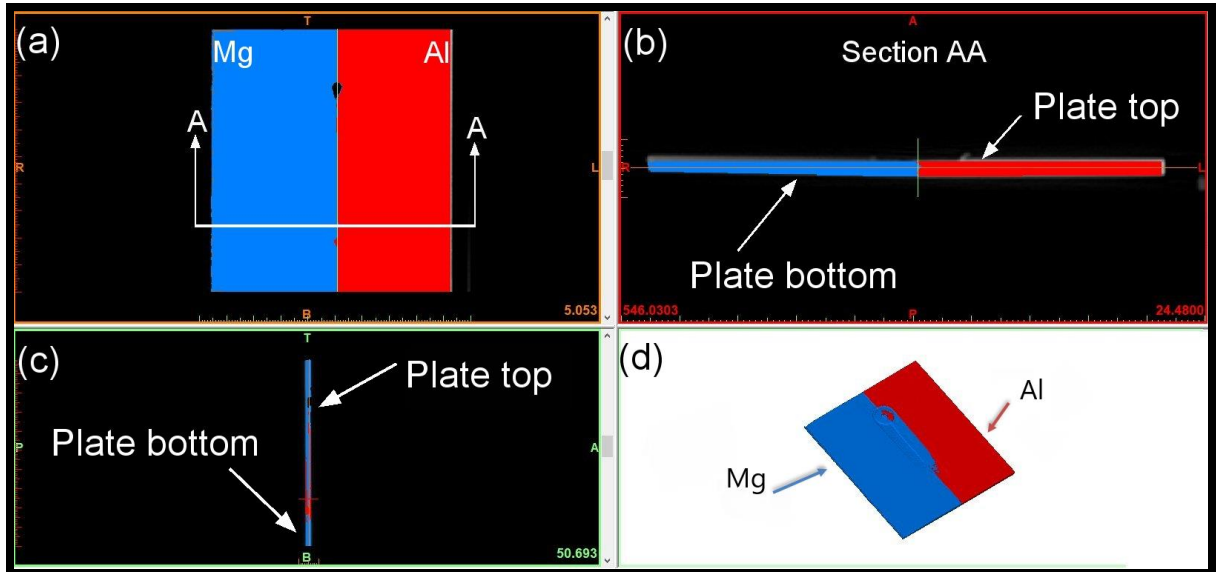


Figure 14 Segmented CT images of sample (f), “Al” and the color red indicated the AA606-T6 alloy, “Mg” and the color blue indicate the AZ31b alloy, (a) top view, (b) cross-sectional view at the section location shown in (a), (c) lateral section across the entire weld length, (d) 3d rendering of the two plates.

Figure 15 shows cross-section A-A of the weld. The centerline of the weld is shown in white, and the material penetration is indicated with arrow marks. The material mixing analysis shows an oblique interface with the AZ31b penetration into the Aluminum alloys taking place at about 1mm below the top of the plate, the maximum penetration of the AA6061-T6 into the magnesium alloy taking place at 0.3mm from the top of the plate. The maximum penetration depths for this cross-section are recorded as 0.6mm from the weld centerline for both alloys. No defects were detected in the weld, aside from a small tunneling defect connected to the exit hole that penetrated 3mm into the weld. This defect is not considered internal since it can be detected by visual inspection by looking into the exit hole. The NDT testing is still beneficial however since the CT X-ray scan can be used to measure the volume of the defect as well as the penetration depth into the weld.

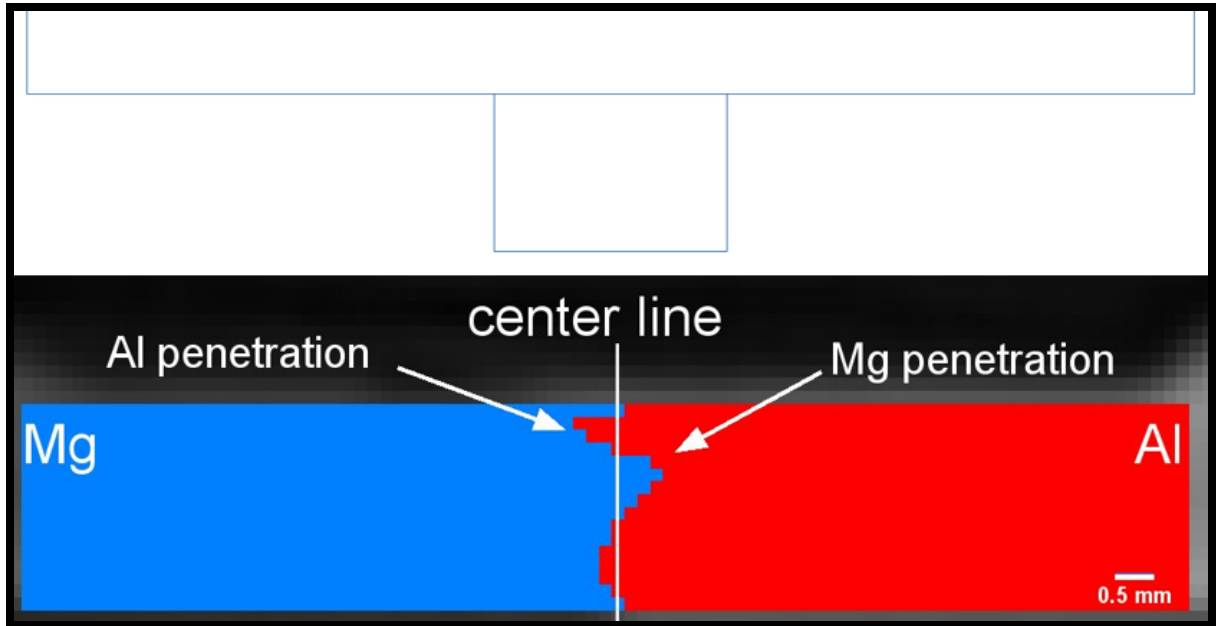


Figure 15 Zoomed-in view of cross-section A-A (bottom) the centerline is shown with a vertical white line, the material mixing is highlighted with arrows, (top) outline of the tool used for sample (f) shown at the same scale.

Figure 16 shows the 3D model of the weld sample. The material transfer at the top surface of the weld is clearly shown, measurements of the material transfer show that the  $103 \text{ mm}^3$  of the AZ31b alloy was transferred to the aluminum alloy plate, while  $31 \text{ mm}^3$  of the AA6061-T6 was transferred to the magnesium alloy. This may be attributed to the fact that compared to sample (e), sample (f) had the AZ31b as the advancing plate and since it is the softer of the two materials a more substantial material transfer was observed for the AZ31b alloy on the top surface of the plate.

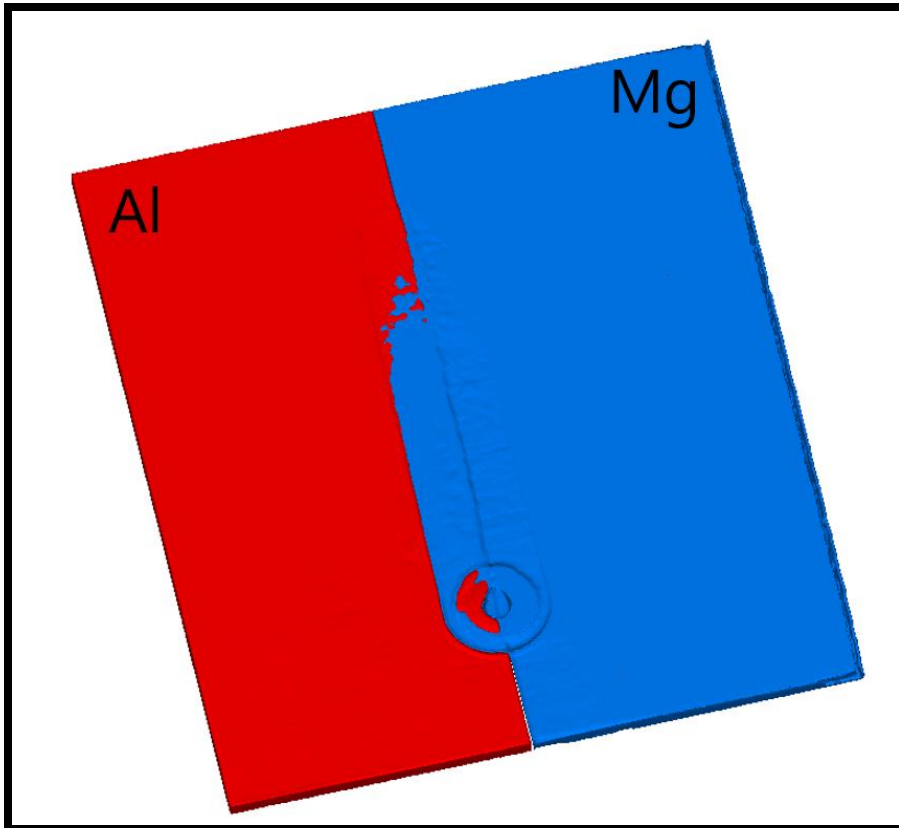


Figure 16 3D rendering of weld sample (f) the top surface AZ31b material deposit is evident.

### **E. NDT Analysis Using Reconstructed Images:**

The above analysis of samples (e) and (f) was performed again using reconstructed CT images at a higher resolution; this was done to study the effect of higher pixel resolution on the NDT analysis. The reconstruction of the images was performed using “MIMICS” using the “IMAGE RESLICE” command. The image reconstruction was applied on all CT images of each sample the slice spacing was kept the same, and the pixel size was set to 50 microns. The Otsu thresholding was then applied to all cross-sections in the same manner described in section C and D of this chapter; the same location area was used for both samples. This section aims to explore the reconstructed images as a possible

method to further improve the resolution of a CT X-ray scan beyond the initial scan resolution, and the effect of doing so on the detected internal defects and mixing interfaces.

### 1. NDT Analysis Using Reconstructed Images of Sample (e)

Figure 17 shows the HU histogram of the reconstructed images of sample (e). The same profile as the HU histogram of the original section shown in figure 13 is observed here. The trimodal peaks are still present. The Otsu thresholds obtained are 54 and 1159 HU, compared to the Otsu thresholds for the original section (56 and 1162 HU), this is a change of 3.7% 0.25% respectively for the two thresholds. The reliability measure for this segmentation is 0.92 vs. 0.918 for the original section ,an improvement of 0.217%.

The mean and standard deviation values for the three segmented regions showed similar miniscule changes in values.

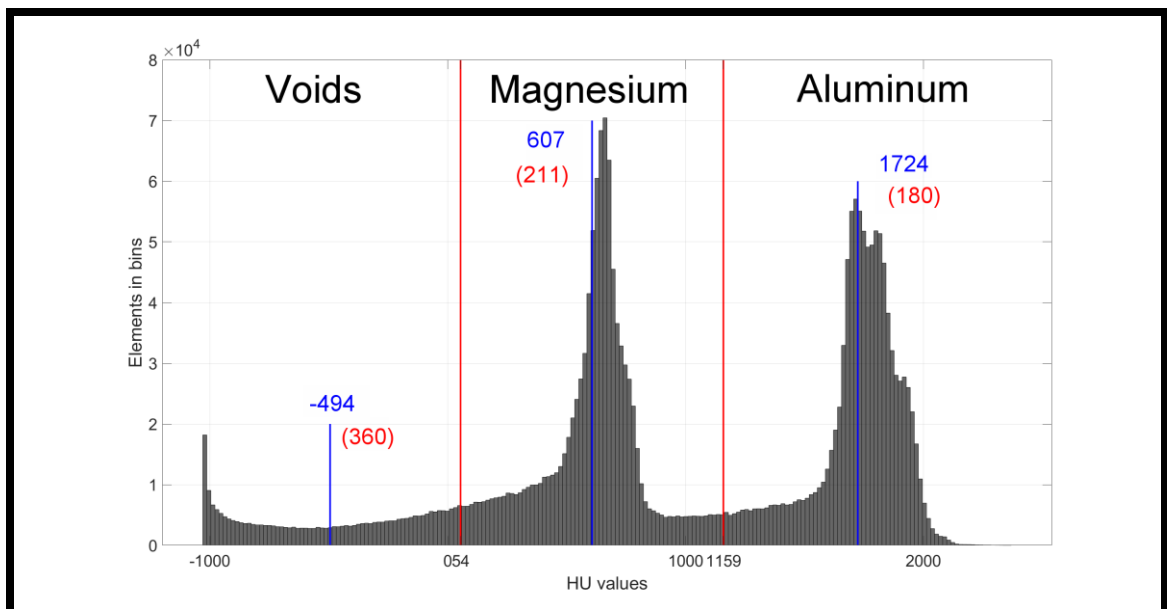


Figure 17 HU level histogram of reconstructed images of weld sample (e). the threshold value indicated by a red vertical line, each segment is labeled, the average HU value for each segment is shown in blue and indicated by a blue line, the standard deviation values are shown in brackets

The reconstructed cross-section A-A for sample (e) is shown in figure 18, the same features as the original cross-section are present. The features, however, have a more gradual profile due to the higher pixel density. This results in a change in the measured areas. The cross-section of the tunneling defect now has a measured area of  $2.87\text{mm}^2$  an increase of 9% over the original areal measurement. The AA6061-T6 deposit, as well as the penetration at the bottom, present a more definite shape as well. As for the volume of the tunneling defect, the same overall shape is observed as the one shown in section C; however, the volume measurement showed an increase of  $5.6\text{mm}^3$  over the original measurement of  $180\text{mm}^3$ , an increase of 3%. Calculating the tunnel volume from the tunnel mask results in a volume of  $182\text{mm}^3$  this is calculated based on the number of elements in the mask (217690) and the pixel size and slice thickness.



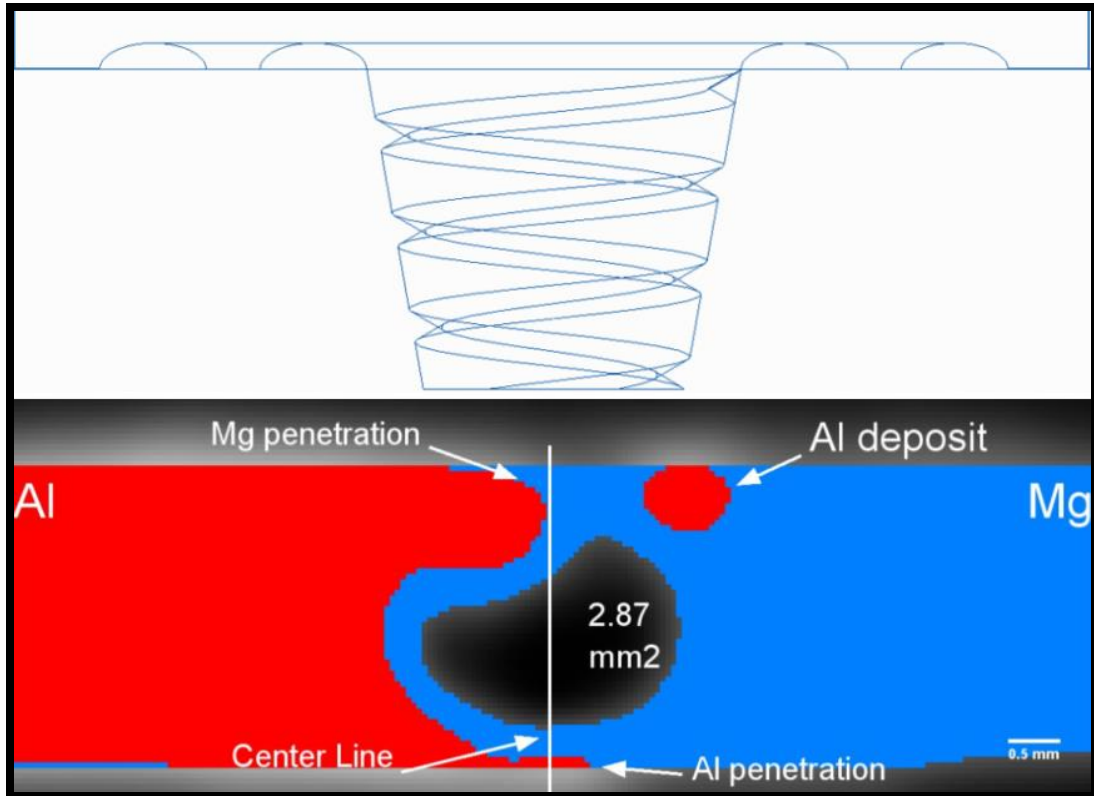


Figure 18 Zoomed-in view of reconstructed cross-section A-A (bottom), the centerline of the weld is marked with a vertical white line. The material mixing is indicated with arrows; the defect area is shown, (top) outline of the tool used for sample (e) shown at the same scale.

## 2. NDT Analysis Using Reconstructed Images of Sample (f)

The same analysis is repeated for sample (f). Figure 9 shows the HU histogram, again compared to the histogram of the original sample, nearly the same values for the thresholds, averages, and standard deviations are observed. The histogram shows a more gradual distribution around the peaks, and this is due to the increased pixel density resulting in more elements spanning the HU range for each segment more evenly. The HU threshold value calculated is 1091, with an effectiveness measure of 0.890. Compared to the original threshold of 1082HU and effectiveness measure of 0.871, the HU threshold varied by 0.831% and the effectiveness measure improved by 2.18%.

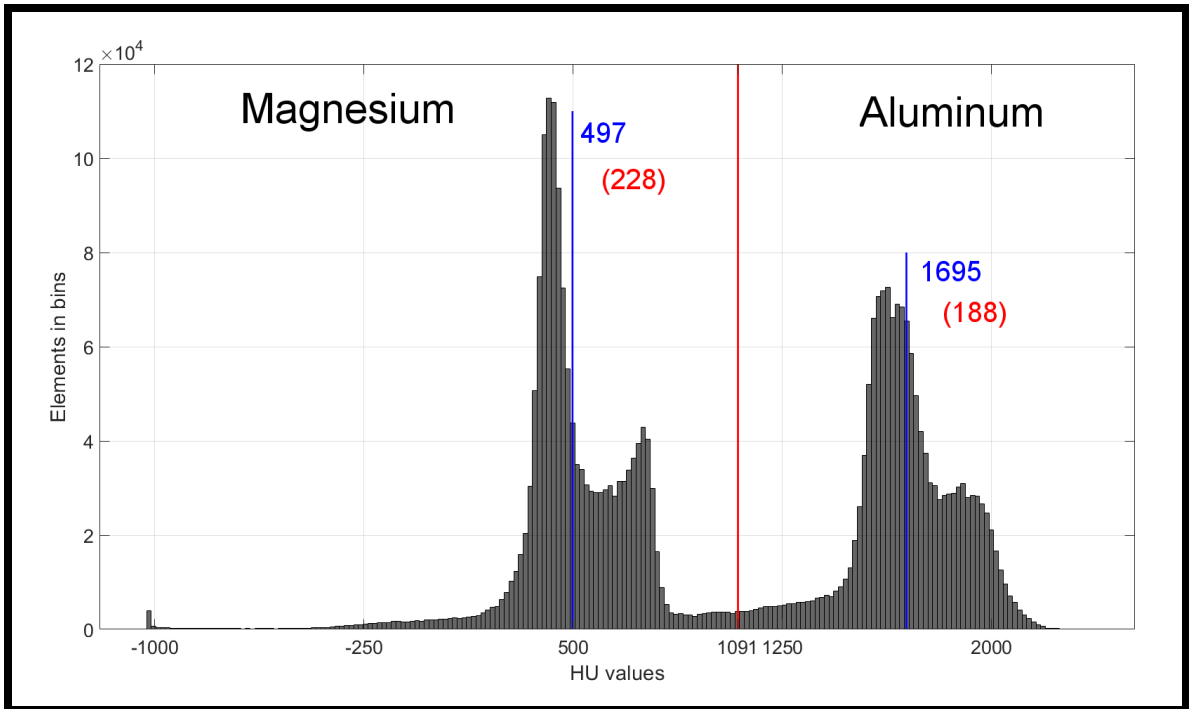


Figure 19 HU level histogram of reconstructed CT images of weld sample (f). The threshold value indicated by a red vertical line, each segment is labeled, the average HU value for each segment is shown in blue and indicated by a blue line, the standard deviation values are shown in brackets.

Figure 20 shows the reconstructed cross-section A-A of sample (f), the mixing interface between the materials has the same rough shape as the original cross-section however near the bottom half of the sample more AZ31b penetration is observed. The maximum AZ31b penetration into the aluminum alloy plate is still measured as 0.6mm from the centerline. The maximum AA6061-T6 is 0.5mm, showing a 0.1mm decrease from the recorded measurement on the original cross-section.

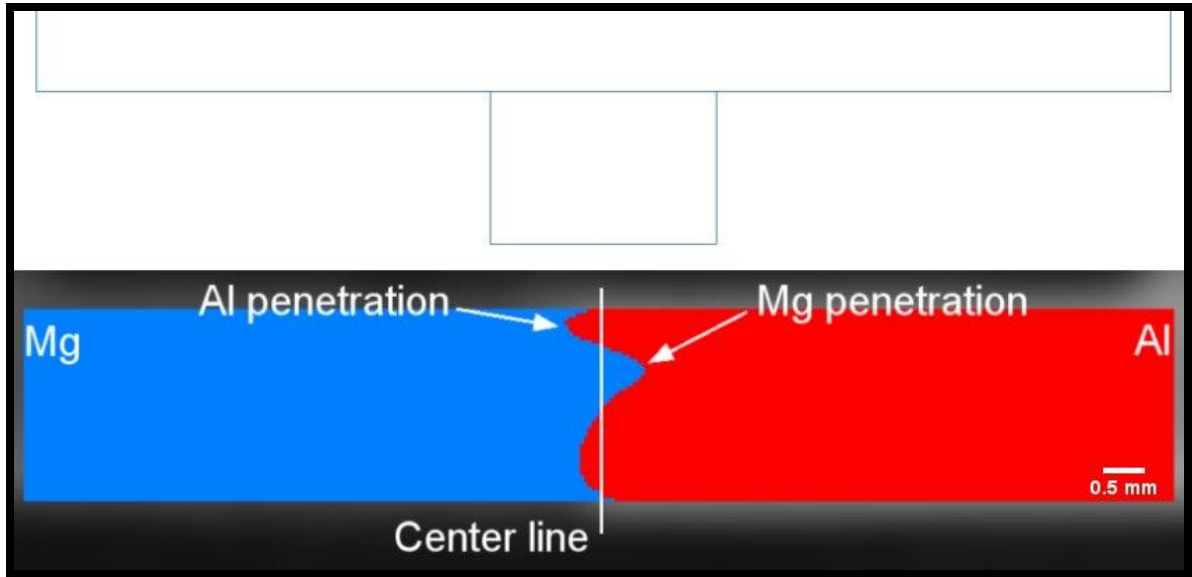


Figure 20 Zoomed-in view of the reconstructed cross-section A-A (bottom) the centerline is shown with a vertical white line, the material mixing is highlighted with arrows, (top) outline of the tool used for sample (f) shown at the same scale.

It is concluded that the higher resolution reconstruction does not present any negative or undesirable effect on the segmentation and NDT analysis and does result in better images due to the higher resolution obtained. Reconstruction can be used as a way to further increase the resolution of the CT images for a better NDT while being within a 10% error margin of the original section; the error percentage may vary however depending on the measurement as well as the range of change in resolution.

## CHAPTER IV

### SEM/EDX DESTRUCTIVE VERIFICATION

In order to verify the obtained results of the NDT CT X-ray analysis, destructive analysis using SEM and EDX was performed. SEM was used to obtain high-resolution images of the cross-sections and to verify the location and shape of the internal defects. EDX was used to verify the results of the NDT mixing evaluation.

#### **A. SEM/EDX Setup and Parameters**

The SEM used for this analysis is the MIRA3 developed by TESCAN; the EDX scanner used is the 20mm<sup>2</sup> detector developed by OXFORD INSTRUMENTS. The scanning parameters are listed in table 5. The methodology for the analysis is as follows; First, the sample is cut around the indicated cross-section location (sections A-A), and then ground to the exact position of the cross-section. The grinding process is followed by three-stage polishing to ensure an excellent surface finish is obtained for the elemental composition tracking; the sample is then cleaned with ethanol and rinsed with deionized water to ensure that no contaminants are present on the cross-section, the sample is dried using dry compressed air before placing in the SEM chamber.

The defect verification was performed by utilizing the high-resolution images of the SEM and analyzing the position and shape of the detected defects and comparing them to those obtained by the NDT method. The mixing analysis was accomplished by tracking

the concentration of magnesium and aluminum using two methods and comparing the results against those obtained by the NDT analysis. The first method is performed by using points spectrums organized in an orthogonal grid of size 15x25, at each element a 30 second EDX scan is performed to obtain the elemental composition at that position, this is then compared to the baseline composition of the pure alloys used in order to determine the degree of material penetration and transfer. The second method is via the “MAPPING” function in the MIRA EDX software; this function creates an elemental map of the of entire cross-section by placing a dot at each location a particular element is detected, the mapping analysis was stopped at a point count of 50000. Both analyses are performed using the maximum field of view of the SEM at the required z-axis position for the EDX analysis which is 15mm. This results in a field of view of about 7.3 to 7.5mm depending on the sample positioning and Wd calibration accuracy.

Table 5 SEM/EDX key parameters

Parameter	value
Voltage	5 - 7 KV
Current	119e-3 nA
Resolution	7 nm
Wd	15mm
Spectrum scan time	30s
Chamber pressure	86.114E-3 Pa
Field of View	7-7.5mm
Interaction area	72nm

## **B. SEM/EDX Destructive Analysis of Sample (e)**

The destructive analysis is performed on cross-section A-A of sample (e) using the two methods described above. Figure 21(a-b) shows cross-section A-A obtained from the NDT analysis, figure 21 (c) shows the SEM images of the actual cross-section A-A overlaid with the results of the point spectrum analysis for the aluminum element. The percentage by weight of aluminum detected is showed using colored points placed at the scan location of the EDX analysis. The AA6061-T6, as expected, shows the aluminum concentrations in the 90% to 100% range, and the AZ31b shows aluminum concentrations in the 0% to 10% range. For the weld zone, however, the destructive analysis confirmed the presence of the aluminum deposit detected in the NDT analysis. The destructive analysis also verified the presence of the bottom aluminum penetration in the AZ31b plate. However, this penetration is more pronounced than what the NDT shows, this is attributed to the averaging process of the HU values between the air and AA6061-T6 plate resulting in HU values within the AZ31b HU range such that the AA6061-T6 penetration is shown in a less pronounced manner than that of the NDT results. As for the AZ31b penetration, figure 22 (c) shows the elemental tracking of the magnesium element along the same cross-section and using the scanning locations. The magnesium mixing shows to the left-center of the weld line between the tunneling defect, and the AA6061-T6 plate is verified by the magnesium concentration detected for 5 points in that region. These 5 points show the same magnesium concentration for the base plate. It is noted that the magnesium concentration for the base plate is below the expected 96%, with the average magnesium range for the scanned points ranging between 60% to 70% range, this attributed to the

presence of carbon contaminates what were not thoroughly rinsed, this was corrected for the later destructive tests, however since the detected magnesium elemental percentage in the transferred segment matches that of the base AZ31b plate the analysis still holds.

Figure 23 shows the results of the elemental mapping analysis of sample (e). Figure 23 (a) shows the location of the EDX scan; it can be seen that the tunneling defect is filled with material shavings or filaments, due to the plastic shearing action taking place and poor mixing. Figure 23 (b) shows the aluminum elemental mapping, as noted from the point spectrum analysis the aluminum deposit is present, the elemental mapping allows for a more definite shape to be visualized, it also noted that to the left of the centerline. At the middle of the cross-section the sheared off filament is mostly aluminum as indicated by the color red; however, some magnesium is detected that is above the baseline concentration of the AA6061-T6 alloy as is shown in figure 23 (c). At the bottom of this filament and above it is also noted that there is some magnesium present, showing that the segmentation in that area is correct, but due to the averaging process, the mixing appears more pronounced in the CT X-ray scans.

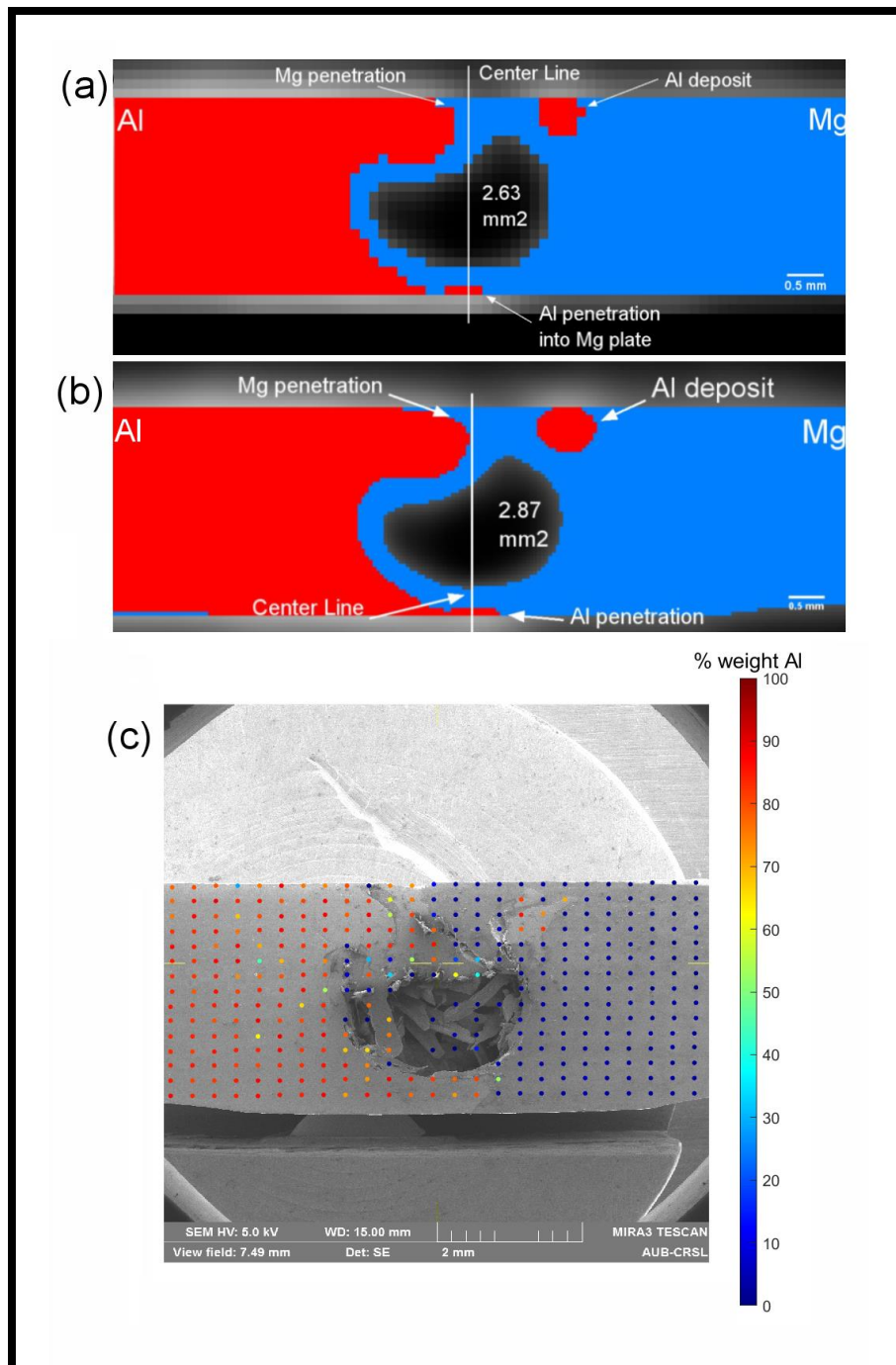


Figure 21 Destructive validation of sample (e). (a) Original cross-section A-A, (b) reconstructed cross-section A-A, (c) SEM images of cross-section A-A overlaid with the EDX point spectrum analysis results. The color bar indicated the percentage of aluminum detected.



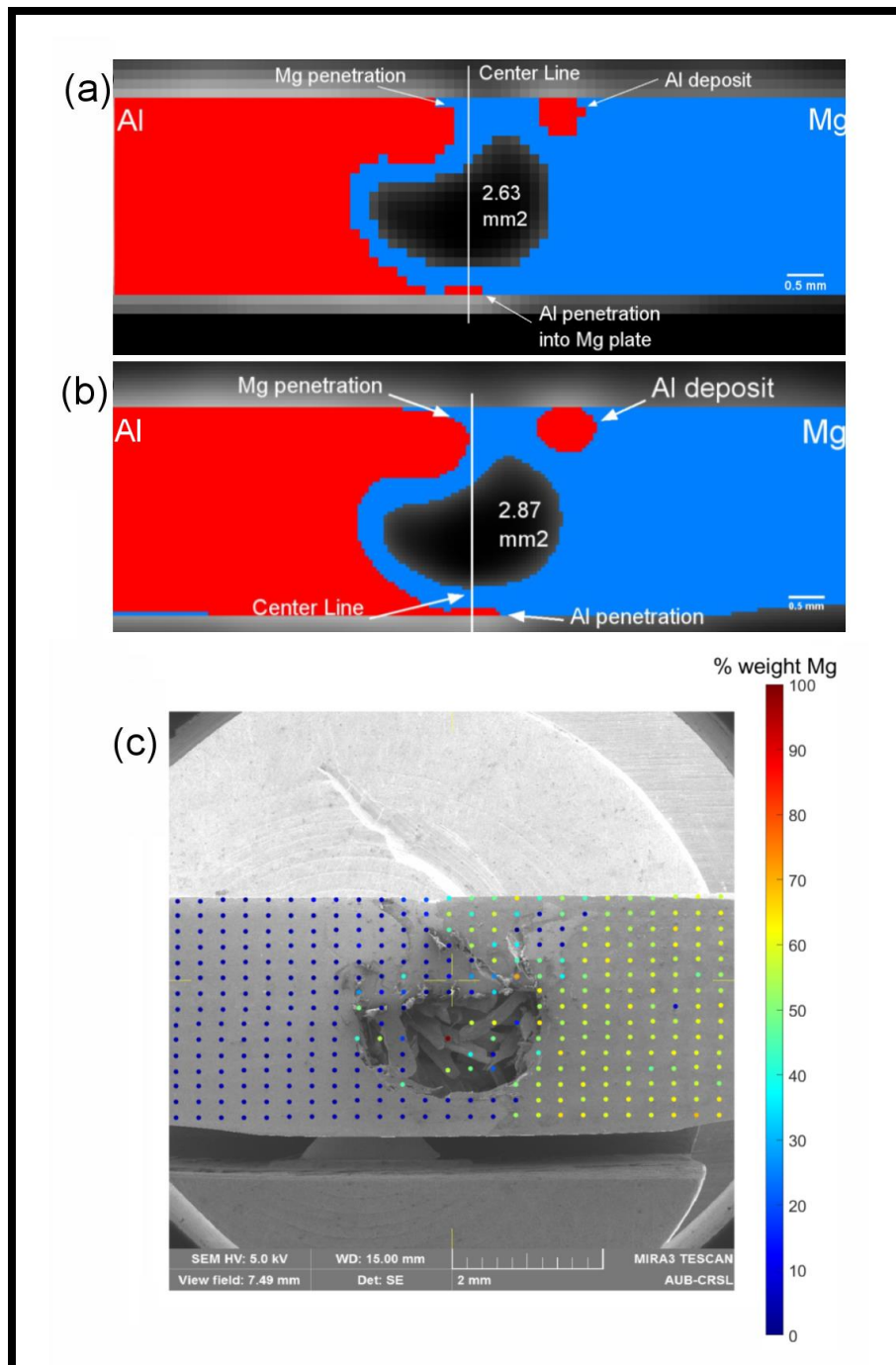


Figure 22 Destructive validation of sample (e). (a) Original cross-section A-A, (b) reconstructed cross-section A-A, (c) SEM images of cross-section A-A overlaid with the EDX point spectrum analysis results. The color bar indicated the percentage of magnesium detected

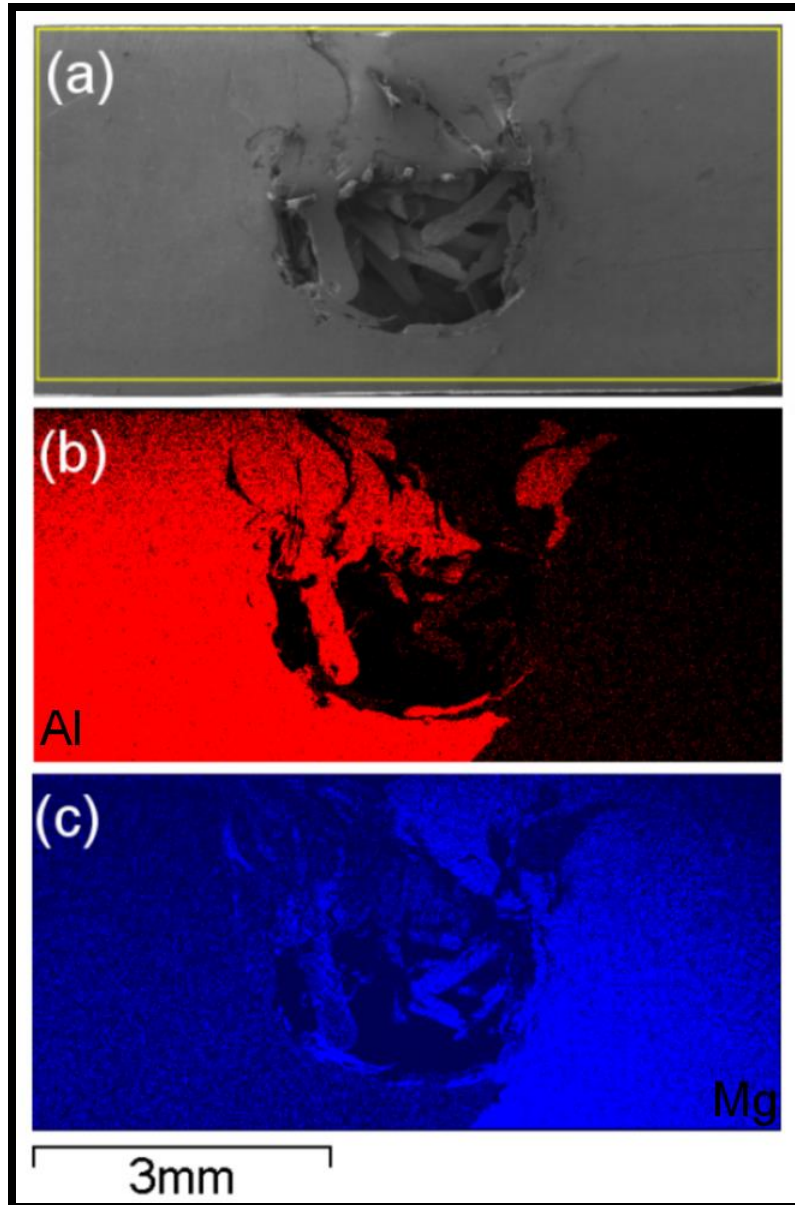


Figure 23 Elemental mapping destructive verification of sample (e). (a) cross-section A-A a yellow rectangle indicates where the mapping analysis was performed. (b) aluminum map, red indicates high aluminum detection. (c) magnesium map, blue indicates high magnesium detection.

### C. SEM/EDX Destructive Analysis of Sample (f)

Figures 24 and 25 (a) and (b) show cross-section A-A from the original scan and reconstructed scan for sample (f), respectively. Figure 24-25 (c) shows the point spectrums analysis results for the aluminum and magnesium elements respectively, with the blue color indicating zero % detection and dark red indicating 100% detection. As is shown in figure 24-25 (c) the baseline concentrations for the base metals are in line with what is expected, for AA6061-T6 alloy the Al concentration is within the 90-100% range, while for the AZ31b alloy the magnesium percentage is also within the 90-100% magnesium range. The overall shape of the interface is corroborated by the elemental analysis, figure 24-25 (c) shows the oblique interface shape detected in the X-ray CT scans. For the original CT cross-section while the shape is accurate to that of the destructive verification the AA6061-T6 penetration at the top of the weld shows that the top pixels are AZ31b which is inaccurate as is evident from figure 24-25 (c). For the reconstructed cross-section, the AA6061-T6 penetration shape is more in line with the results of the destructive analyses. These false-positive AZ31b pixels are attributed to the averaging process described above, the higher pixel count of the reconstructed segment mitigates the effect of this problem and leads to more accurate results. Figure 24-25 (c) shows that the AZ31b penetration is in line with that recorded from the NDT X-ray CT analysis, but for the bottom section of the weld the interface where there was no plastic deformation due to the difference in length between pin (2mm) and sample (3mm), figures 24-25 (c) show a vertical interface, but the NDT analysis shows a more curved interface. This may be attributed to the edges having protrusions from the sample preparation steps before

welding, leading therefore to micro gaps that affect the accuracy of the X-ray CT in that location.

Figure 26 shows the elemental mapping analysis for sample (f). Figure 26 (a) shows the location where the scan was performed. Figure 26 (a) and (b) shows the elemental map for the aluminum and magnesium elements respectively. The mapping analysis results show the same interface structure as the point spectrum analysis, but with a higher level of details. For example, figure 26 (b) shows the two aluminum deposits in the AZ31b plates indicated with yellow rectangles, figure 26 (c) corroborates that with lack of blue color at those two locations. At the bottom of the pin length a higher concentration of aluminum compared to the base aluminum concentration of the AZ13b alloy, indicative of material transfer at that location, this is indicated by a blue rectangle in figure 26 (b). As for the penetration measurements, the maximum recorded penetration for both samples measured 1mm from the center-line, compared to the measurements obtained in section D of this chapter that is a 0.4mm error. This error can be mitigated by further increasing the scanning and reconstruction resolution of the CT images.

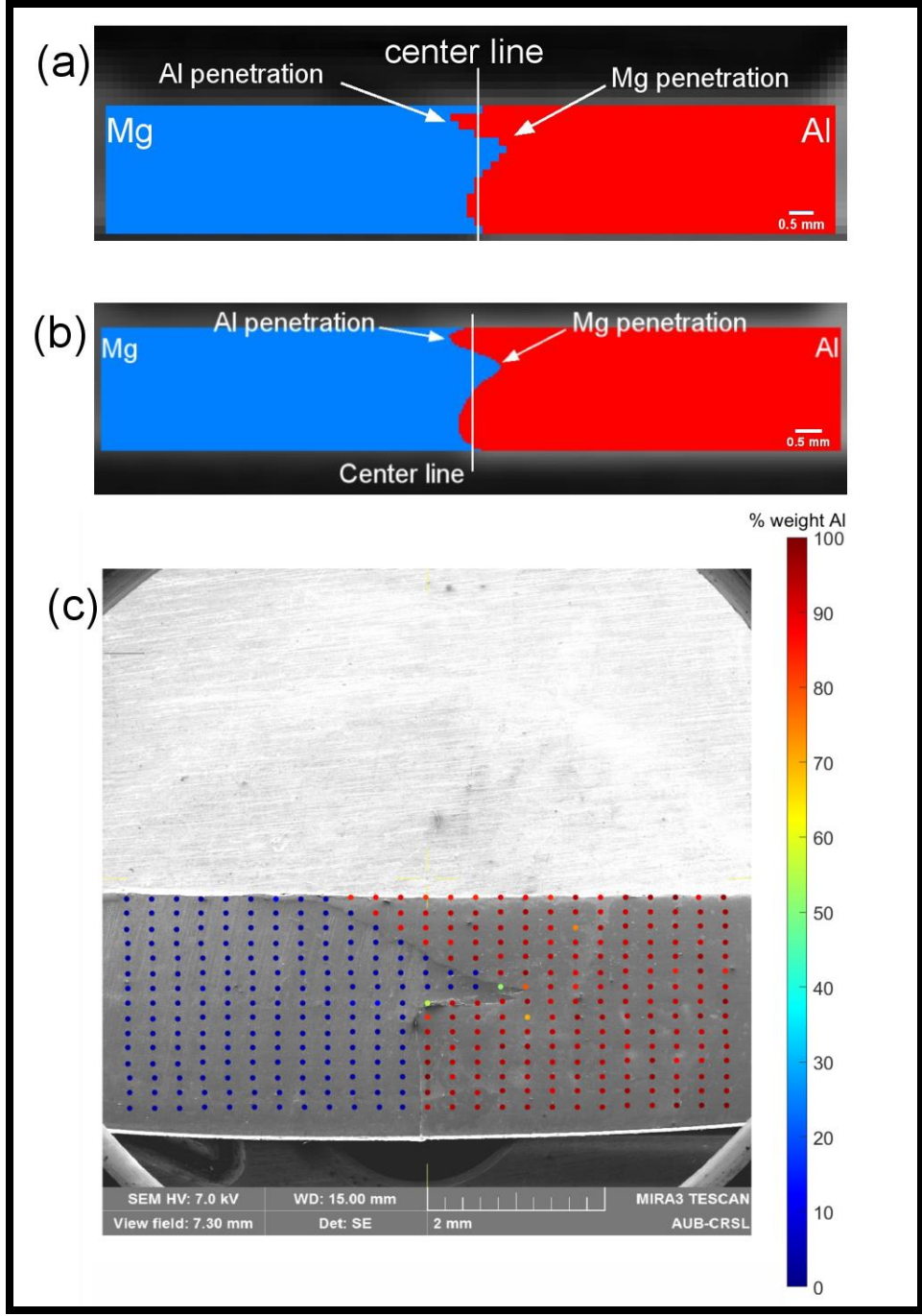


Figure 24 Destructive validation of sample (f). (a) Original cross-section A-A, (b) reconstructed cross-section A-A, (c) SEM images of cross-section A-A overlaid with the EDX point spectrum analysis results. The color bar indicated the percentage of aluminum detected.

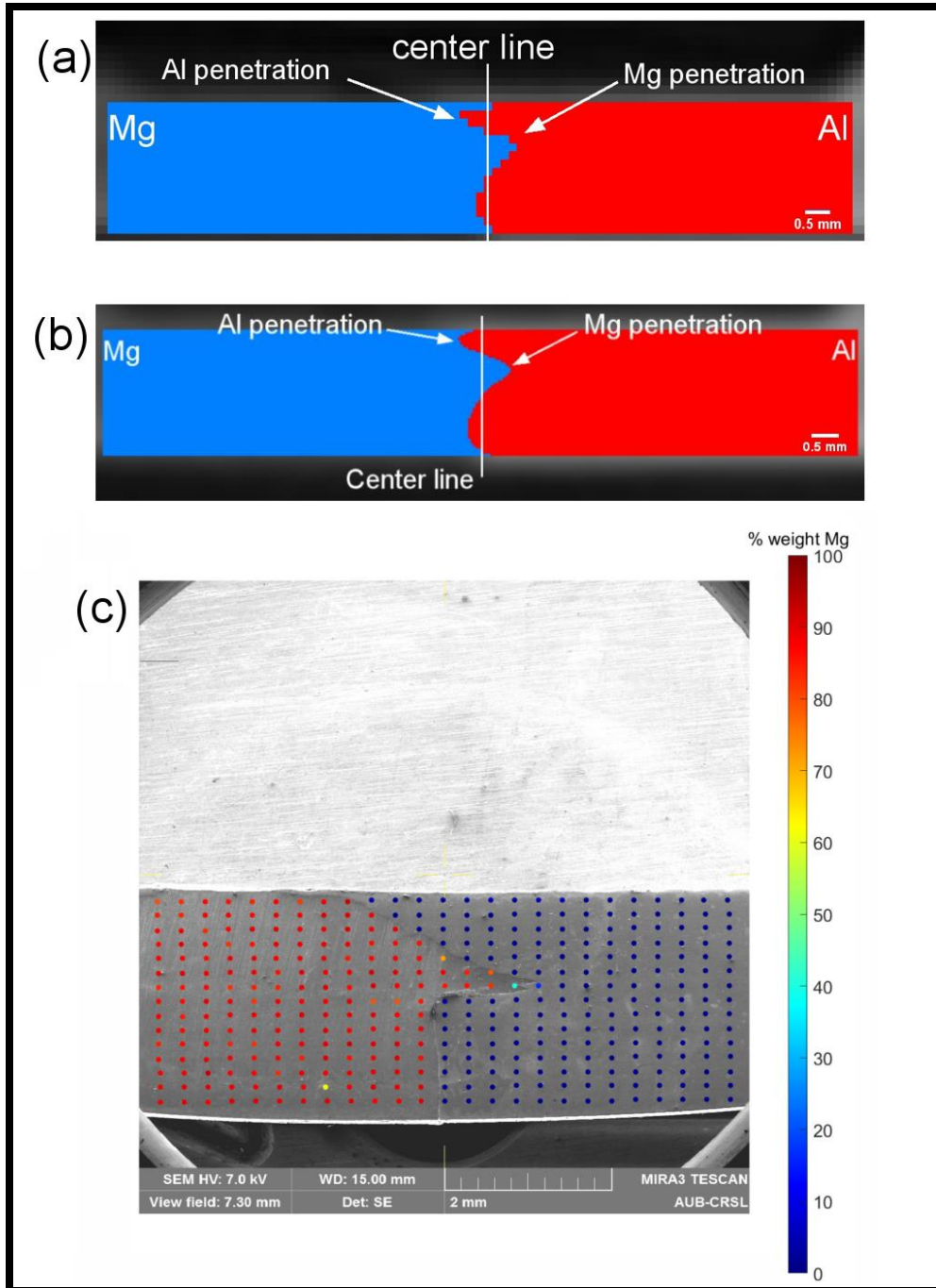


Figure 25 Destructive validation of sample (f). (a) Original cross-section A-A, (b) reconstructed cross-section A-A, (c) SEM images of cross-section A-A overlaid with the EDX point spectrum analysis results. The color bar indicated the percentage of magnesium detected.

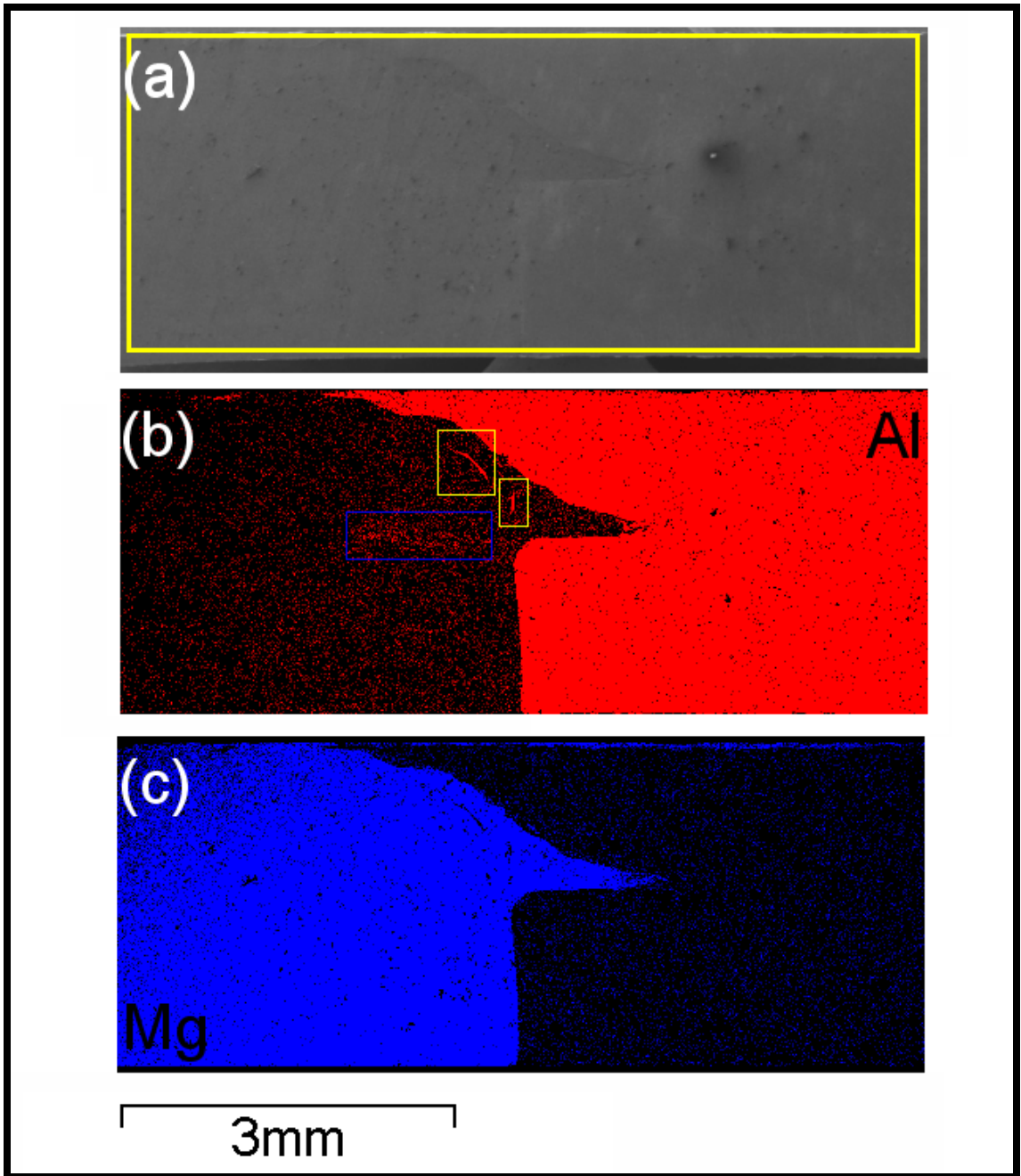


Figure 26 Elemental mapping destructive verification of sample (f). (a) cross-section A-A a yellow rectangle indicates where the mapping analysis was performed. (b) aluminum map, red indicates high aluminum detection. (c) magnesium map, blue indicates high magnesium

## CHAPTER V

### DISCUSSIONS AND CONCLUSIONS

In this work, a method for the non-destructive analysis for the detection and analysis of internal defects and mixing based on the X-ray computed tomography, and the Otsu image thresholding technique was developed, tested, and corroborated. This method was able to accurately detect defects and quantify material mixing in friction stir welded dissimilar AA6061-T6/ AZ31b butt joints.

Multiple tools were tested in order to produce suitable welds that were analyzed using the developed method. It was found that friction stir welding of dissimilar AA6061-T6/ AZ31b using multiple tool geometry, this, however, depends significantly on the proper selection of the welding parameters for each tool geometry. Sample (f) was the best welded sample performed at a rotational tool speed of 1400RPM and welding feed of 300mm/min using a cylindrical FSW tool with a small diameter pin.

The NDT method was tested on two of the samples that showed interesting cross-sections. Samples (f) and (e) were analyzed using both direct X-ray CT images as well as higher resolution reconstructed X-ray CT images, both image types were able to capture the shape and location of the defect and mixing accurately, with the reconstructed images showing better accuracy for shape determination. The reconstructed sections resulted in an improvement in the accuracy of the OTSU thresholding method, with sample (e) showing an improvement of 0.217% and sample (f) showing an improvement



of 2.18%. Figure 27 shows the histogram of the original and reconstructed NDT analysis of sample (e), the total number of elements analyzed for the original and reconstructed sections are 338800 and 2349696, respectively. This increase in number of element number of nearly 7 times, is the main reason for the Otsu accuracy improvement. The histograms of sample (e) show a similar shape for the peaks and valleys. The histograms also showed nearly the same values for the mean, and no significant improvements were measured for the standard deviations for this sample.

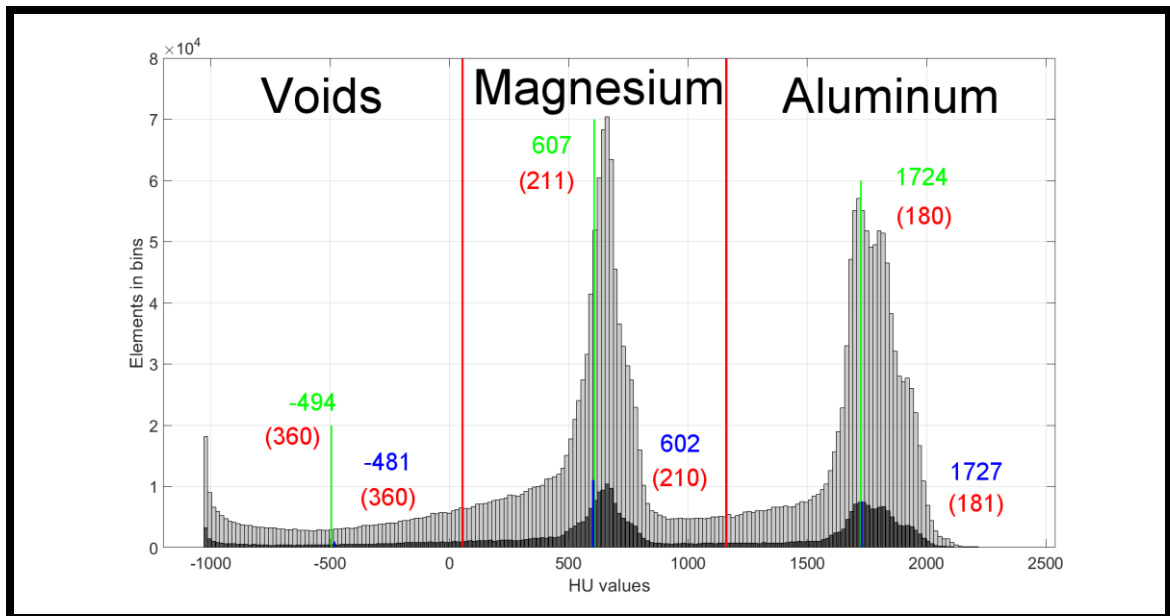


Figure 27 Otsu HU histogram of sample (e), transparent black: histogram of the reconstructed cross-sections, solid black: histogram of the original cross-sections.

Figure 28 shows the overlaid histograms of sample (f), for this sample as well the two histograms present the same shape, the increased element number, in this case, resulted in an improvement of 2.18% in the effectiveness measure for the Otsu

thresholding method. the changes in the mean values for each segment changed by 2.89% and 0.35% for the AZ31b and AA6061-T6 respectively, as for the standard deviations, the variations improved by 9.52% and 9.61% respectively for the AZ31b and AA6061-T6 sections. Based on these results, it is concluded that reconstructed sections can be used to achieve better thresholding results as well as increase the shape accuracy of the CT images.

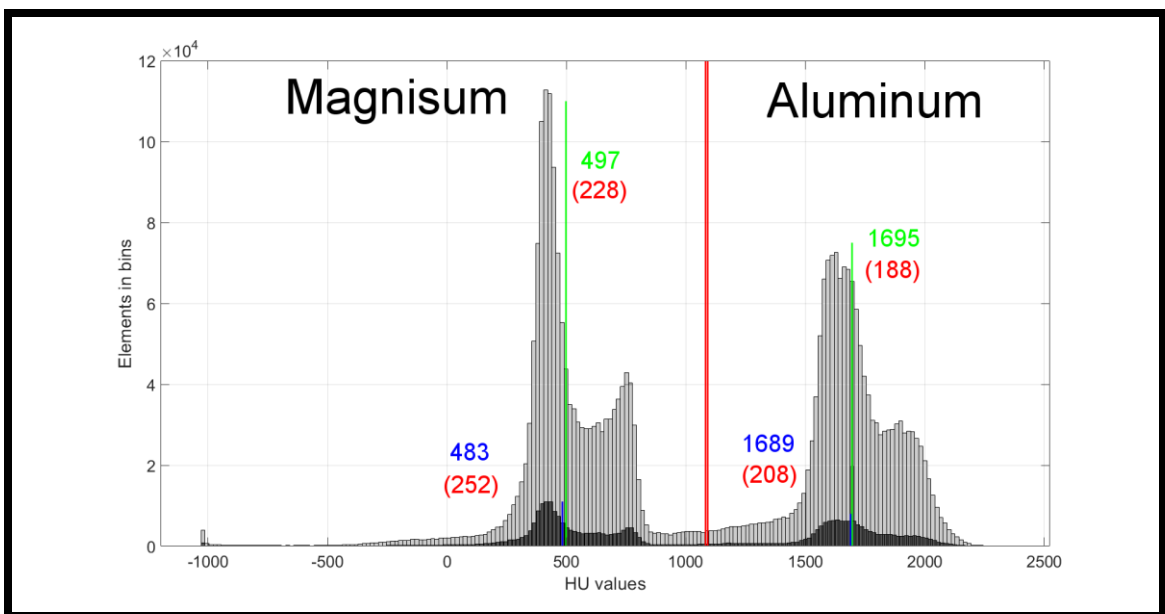


Figure 28 Otsu HU histogram of sample (f), transparent black: histogram of the reconstructed cross-sections, solid black: histogram of the original cross-sections.

The results of the NDT method were verified via two types of EDX analysis, point spectrum, and elemental mapping. The verification showed that the NDT was able to determine the location, size, and composition of features in the weld zone. Figures 29 and 30 (top) shows the combined elemental maps of Aluminum and Magnesium elements obtained by combining the RGB values for both single elemental map images. Figure 28

and 29 (bottom) show the reconstructed cross-sections of both samples. For sample (e) the tunneling defect was successfully detected as well at the aluminum deposit and bottom aluminum penetration into the AZ31b plate. The magnesium penetration on the surface of the AA6061-T6 plate is also detected, as well as the magnesium around the tunneling defect.

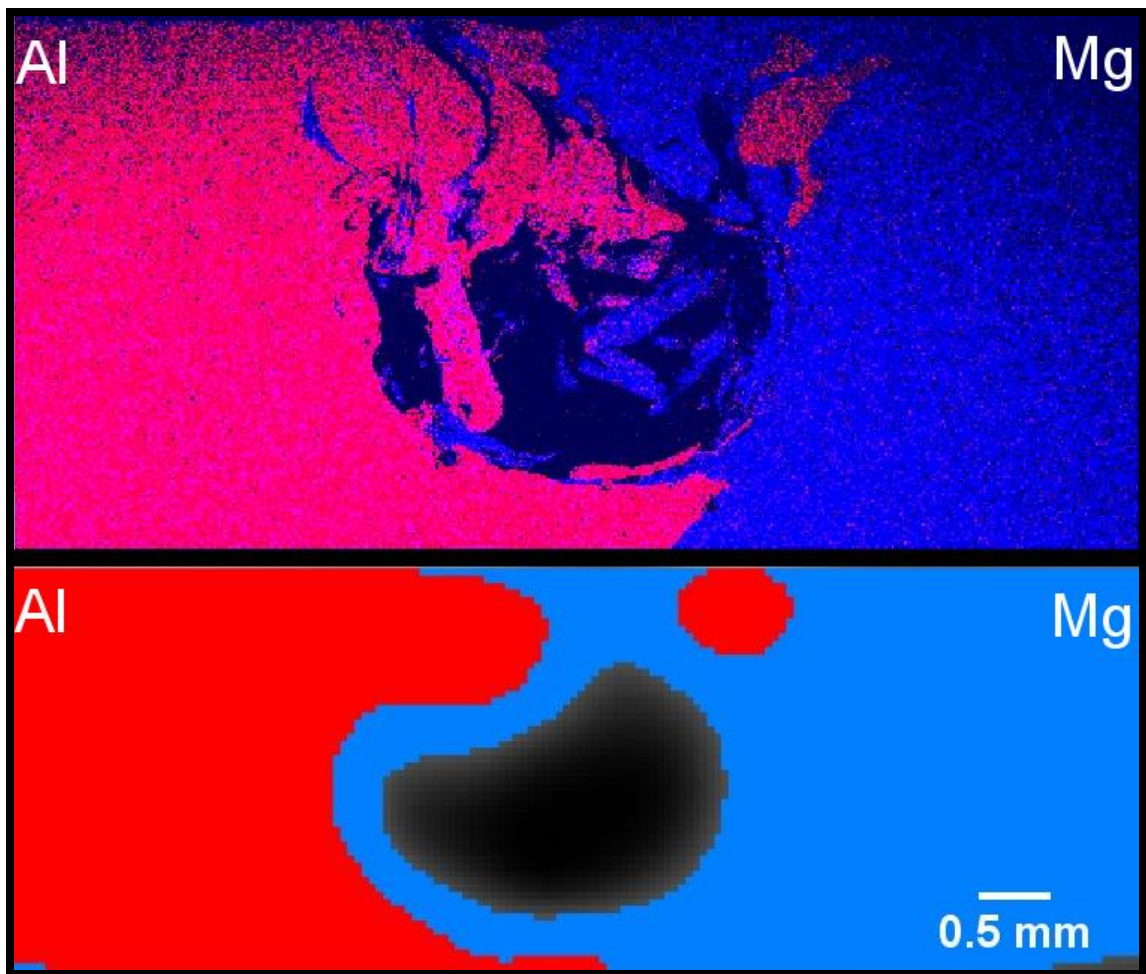


Figure 29 Sample (e), (top) combined EDX elemental analysis of cross-section A-A, (bottom) reconstructed cross-section A-A.

For sample (f) shown in figure 30, the interface shape was accurately detected. The EDX analysis for this sample also shows that at the oblique interface between the two materials the number of violet pixels is larger than that of the vertical interface where no welding took place, this is most evident at the tip of the AZ31b penetration where a large amount of violet pixels is observed, this shows that for those pixels both Al and Mg elements were detected, which may indicate the presence of intermetallic compounds at this location. These violet pixels are also observed in the left filament of tunneling defect shown in figure (29). The presence of these intermetallic compounds in sample 29 can explain the formation of the tunneling defect since the high hardness of the intermetallic compounds can cause excessive shearing actions removing materials from the base metal as they are moved by the welding action.

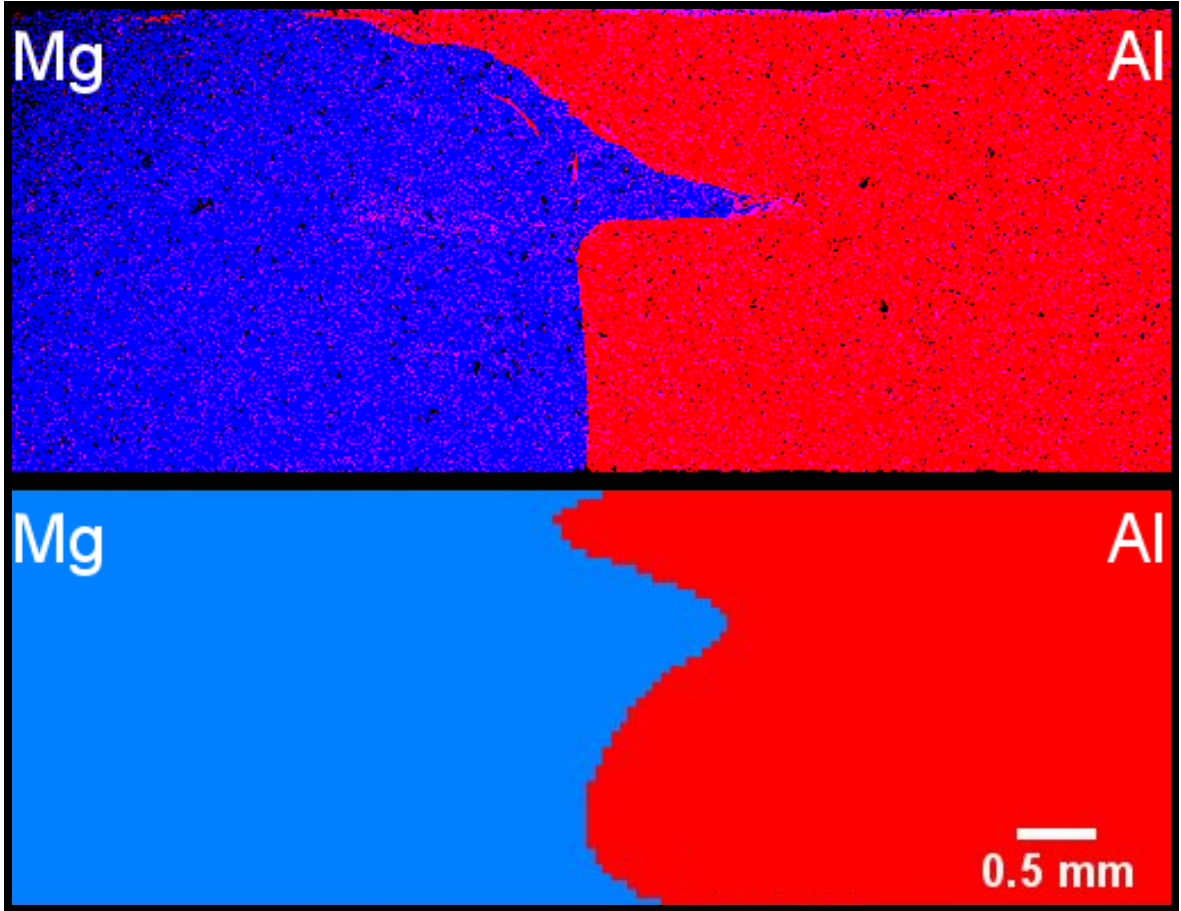


Figure 30 Sample (f), (top) combined EDX elemental analysis of cross-section A-A, (bottom) reconstructed cross-section A-A.

## BIBLIOGRAPHY

- [1] V. Dattoma, R. Nobile, F.W. Panella, A. Saponaro, "NDT Thermographic Techniques on CFRP Structural Components for Aeronautical Application" *Procedia Structural Integrity*, 2018, Volume 8, Pages 452-461.
- [2] R. Yang, Y. He, H. Zhang, "Progress and Trends in Nondestructive Testing and Evaluation for Wind Turbine Composite Blade, Renewable and Sustainable Energy Reviews." 2016, Volume 60, Pages 1225-1250.
- [3] S. Changliang, Z. Hao, D. Shiyun, T. Weixue, "Novel Nondestructive Testing Applications in Old Automotive Engine." *Conference Series: Materials Science and Engineering*, 2017, Volume 182, Pages 012060.
- [4] M. Engelhardt, D. Behne, N. Grittner, A. Neumann, W. Reimche, C. Klose, "Non-destructive Testing of Longitudinal and Charge Weld Seams in Extruded Aluminum and Magnesium Profiles." *Materials Today: Proceedings*, 2015, Volume 2, Issue 10, Part A, Pages 4866-4873.
- [5] C. Petit, E. Maire, S. Meille, J. Adrien, "Two-scale Study of The Fracture of an Aluminum Foam by X-ray Tomography and Finite Element Modeling," *Materials & Design*, 2017, Volume 120, Pages 117-127.
- [6] A. E. Moura, C. C. Dantas, M. S. Nery, J. M. Barbosa, T. L. Rolim, E. A. O. Lima, S. B. Melo, V. A. Dos Santos, "Non-Destructive Evaluation of Weld Discontinuity in Steel Tubes by Gamma Ray CT", *Nuclear Instruments and Methods in Physics Research Section B: Beam Interactions with Materials and Atoms*, 2015, Volume 349, Pages 115-162.
- [7] A. Plessis, P. Rossouw, "X-ray Computed Tomography of a Titanium Aerospace Investment Casting", *Case Studies in Nondestructive Testing and Evaluation*, 2015, Volume 3, Pages 21-26.
- [8] S. Zheng, J. Vanderstelt, J.R. McDermid, J.R. Kish, "Non-Destructive Investigation of Aluminum Alloy Hemmed Joints Using Neutron Radiography and X-ray Computed Tomography", *NDT & E International*, 2017, Volume 91, Pages 32-35
- [9] P. Hermanek, S. Carmignato, *Porosity Measurements by X-ray Computed Tomography: Accuracy Evaluation Using a Calibrated Object*, *Precision Engineering*, 2017, Volume 49, Pages 377-387.
- [10] T. W. Morris, N. E. David, N. J. Christopher, M. M. George, T. Peter, D. C John, "Improvements Relating to Friction Welding." 0615480B1 EU Patent, 11 27, 1992.

- [11] M. Venkatesh Kannan, M. Arivarsu, M. Manikandan, N. Arivazhagan, "Review on Friction Welding of Steels." *Materials Today: Proceedings*, 2018, Volume 5, Issue 2, Pages 13227-13235.
- [12] S. K. Tiwari, Dinesh Kumar Shukla, R. Chandra." Friction Stir Welding of Aluminum Alloys: A Review." *International Journal of Materials and Metallurgical Engineering*, 2013, Volume 7.
- [13] K. Singh, G. Singh, H. Singh, "Review on Friction Stir Welding of Magnesium Alloys." *Journal of Magnesium and Alloys*, 2018, Volume 6, Issue 4, Pages 399-416.
- [14] K. Gangwar, M. Ramulu, "Friction Stir Welding of Titanium Alloys: A Review." *Materials & Design*, 2018, Volume 141, Pages 230-255.
- [15] M.M Ahmed, S. Ataya M.M El-Sayed Sleman, H. Ammar, "Friction stir welding of similar and dissimilar AA7075 and AA5083." *Materials Processing Technology*, 2017, Volume 242, Pages 77-91.
- [16] Y. Huang, X. Meng, Y. Wang, Y. Xie, L. Zhou, "Joining of Aluminum Alloy and Polymer Via Friction Stir Lap Welding." *Journal of Materials Processing Technology*, 2018, Volume 257, Pages 148-154.
- [17] R. Murugan, N. Thirumalaisamy, "Experimental and Numerical Analysis of Friction Stir Welded Dissimilar Copper and Bronze Plates." *Materials Today: Proceedings*, 2018, Volume 5, Issue 1, Part 1, Pages 803-809.
- [18] X. He, F. Gu, A. Ball, A Review of Numerical Analysis of Friction Stir Welding, *Progress in Materials Science*, 2014, Volume. 65, Pages 1-66.
- [19] J. Buha, R. N. Lumley A. G. Crosky," Microstructural Development and Mechanical Properties of Interrupted Aged Al-Mg-Si-Cu Alloy", *Metallurgical and Materials Transactions A*, 2006, Volume 37, Issue 10, Pages 3119-3130.
- [20] F. Ozturk, A. Sisman, S. Toros, S. Kilic, R.C. Picu, "Influence of aging treatment on mechanical properties of 6061 aluminum alloy", *Materials and Design*, 2010, Volume 31, Issue 2, Pages 972-975.
- [21] F. Nie, H. Dong, S. Chen, P. Li, L. Wang, Z. Zhao, X.Li, H. Zhang, "Microstructure and Mechanical Properties of Pulse MIG Welded 6061/A356 Aluminum Alloy Dissimilar Butt Joints", *Journal of Materials Science & Technology*, 2018, Volume 34, Issue 3, Pages 551-560.
- [22] B.L Mordike, T Ebert, "Magnesium: Properties — applications — potential", *Materials Science and Engineering: A*, 2001, Volume 302, Issue 1, Pages 37-45.

- [23] M. Wang, B.B. He, M.X. Huang, "Strong and Ductile Mg Alloys Developed by Dislocation Engineering", *Journal of Materials Science & Technology*, 2019, Volume 35, Issue 3, Pages 394-395.
- [24] H. Ye, X. Sun, Y. Liu, X. Rao, Q. Gu, "Effect of Ultrasonic Surface Rolling Process on Mechanical Properties and Corrosion Resistance of AZ31B Mg Alloy", *Surface and Coatings Technology*, 2019, Volume 372, Pages 288-298.
- [25] M. Haghshenas, A. P. Gerlich, *Joining of Automotive Sheet Materials by Friction-Based Welding Methods: A Review*, *Engineering Science and Technology an International Journal*, 2018, Volume 21, Issue 1, Pages 130-148.
- [26] Y. Helal, Z. Boumerzoug, L. Fellah, "Microstructural Evolution and Mechanical Properties of Dissimilar Friction Stir Lap Welding Aluminum Alloy 6061-T6 to Ultra Low Carbon Steel", *Energy Procedia*, 2019, Volume 157, Pages 208-215.
- [27] K. Elangovan, V. Balasubramanian, *Influences of Post-Weld Heat Treatment on Tensile Properties of Friction Stir-Welded AA6061 Aluminum Alloy Joints*, *Materials Characterization*, 2008, Volume 59, Issue 9, Pages 1168-1177.
- [28] J. Fathi, P. Ebrahimzadeh, R. Farasati, R. Teimouri, "Friction Stir Welding of Aluminum 6061-T6 In Presence of Watercooling: Analyzing Mechanical Properties and Residual Stress Distribution", *International Journal of Lightweight Materials and Manufacture*, 2019, Volume 2, Issue 2, Pages 107-115.
- [29] N. Xu, Q. Song, H. Fujii, Y. Bao, J. Shen, "Mechanical Properties' Modification of Large Load Friction Stir Welded AZ31B Mg Alloy Joint", *Materials Letters*, 2018, Volume 219, Pages 93-96.
- [30] Y. Han, X. Jiang, S. Chen, T. Yuan, H. Zhang, Y. Bai, Y. Xiang, X. Li, "Microstructure and Mechanical Properties of Electrically Assisted Friction Stir Welded AZ31B Alloy Joints", *Journal of Manufacturing Processes*, 2019, Volume 43, Part A, Pages 26-34.
- [31] P. Gulati, D. K. Shukla, A. Gupta, "Defect Formation Analysis of Friction Stir Welded Magnesium AZ31B Alloy", *Materials Today: Proceedings*, 2017, Volume 4, Issue 2, Part A, Pages 1005-1012.
- [32] X. Meng, Y. Jin, S. Ji, D. Yan, "Improving Friction Stir Weldability of Al/Mg Alloys via Ultrasonically Diminishing Pin Adhesion." *Journal of Materials Science & Technology*, 2018, Volume 34, Issue 10, Pages 1817-1822.



- [33] H. K. Sharma, K. Bhatt, K. Shah, U. Joshi, "Experimental Analysis of Friction Stir Welding of Dissimilar Alloys AA6061 and Mg AZ31 Using Circular Butt Joint Geometry", *Procedia Technology*, 2016, Volume. 23, Pages. 556-572.
- [34] K. P. Mehta, P. Carlone, A. Astarita, F. Scherillo, F. Rubino, P. Vora, "Conventional and Cooling Assisted Friction Stir Welding of AA6061 And AZ31B Alloys", *Materials Science and Engineering: A*, 2019, Volume 759, Pages 252-261.
- [35] W. J. Arbegast, E. R. Coletta, Z. Li, "Characterization of Friction Stir Weld Defect Types." 2001TMS Annual Spring Meeting, New Orleans, LA, February 11-15, 2001.
- [36] P. Kah, R. Rajan, J. Martikainen, R. Suoranta, "Investigation of weld defects in friction-stir welding and fusion welding of aluminium alloys", *International Journal of Mechanical and Materials Engineering*, 2015, Volume 10.
- [37] M. Tabatabaeipour, J. Hettler, S. Delrue, K. Van Den Abeele, "Nondestructive Ultrasonic Inspection of Friction Stir Welds", *Physics Procedia*, 2015, Volume 70, Pages 660-663.
- [38] M. Tabatabaeipour, J. Hettler, S. Delrue, K. V. D. Abeele, "Non-destructive Ultrasonic Examination of Root Defects in Friction Stir Welded Butt-Joints." *NDT & E International*, 2016, Volume 80, Pages 23-34.
- [39] M. J. Santos, J. B. Santos, "Lamb Waves Technique Applied to the Characterization of Defects in Friction Stir Welding of Aluminum Plates: Comparison with X-ray and Ultrasonic C-Scan." *Journal of Testing and Evaluation*, 2010, Volume 38, Issue 5, Pages 622-627.
- [40] F. Schaff, A. Bachmann, A. Zens, M. F. Zaeh, F. Pfeiffer, J. Herzen, "Grating-Based X-ray Dark-Field Computed Tomography for The Characterization of Friction Stir Welds: A Feasibility Study." *Materials Characterization*, 2017, Volume 129, Pages 143-148.
- [41] R. P. Mahto, C. Gupta, M. Kinjawadekar, A. Meena, S. K. Pal, "Weldability of AA6061-T6 And AISI 304 By Underwater Friction Stir Welding." *Journal of Manufacturing Processes*, 2019, Volume 38, Pages 370-386.
- [42] M. Dumont, A. Steuwer, A. Deschamps, M. Peel, P. J. Withers, "Microstructure Mapping in Friction Stir Welds of 7449 Aluminium Alloy Using SAXS", *Acta Materialia*, 2006, Volume 54, Issue 18, Pages 4793-4801.
- [43] C. K. Egan, S. D. M. Jacques, M. D. Wilson, M. C. Veale, P. Seller, P. J. Whithers, J. Cernik, "Full-field Energy-Dispersive Powder Diffraction Imaging Using Laboratory Xrays", *Journal of Applied Crystallography*, 2015, Volume 48, Pages 269-272.

- [44] J. Schneider, R. Beshears, A. C. Nunes, "Interfacial Sticking and Slipping in The Friction Stir Welding Process." *Materials Science and Engineering: A*, 2006, Volumes 435–436, Pages 297-304.
- [45] Y. Morisada, H. Fujii, Y. Kawahito, K. Nakata, M. Tanaka, "Three-Dimensional Visualization of Material Flow During Friction Stir Welding by Two Pairs of X-ray Transmission Systems." *Scripta Materialia*, 2011, Volume 65, Issue 12, Pages 1085-1088.
- [46] R. A. Brook, "A Quantitative Theory of The Hounsfield Unit and Its Application to Dual Energy Scanning." *Journal of Computer Assisted Tomography*, 1977, Volume 4, Pages 487-493.
- [47] M.A. Hurrell, A. P. H. Butler, N. J. Cook, P. H. Butler, J. P. Ronaldson, R. Zainon, "Spectral Hounsfield units: a new radiological concept", *European Radiology*, 2012, Volume 22, Issue 5, Pages 1008-1013.
- [48] N. Otsu, "A thresholding selection method from gray-level histograms." *Automatica*, 1975, Volume 11, Number 285-296, Pages 23-27.
- [49] R.F. Hamade, A.M.R. Baydoun, "Nondestructive detection of defects in friction stir welded lap joints using computed tomography." *Materials & Design*, 2019, Volume 162, Pages 10-23.
- [50] R. F. Hamade, A. Dorbane, G. Ayoub, B. Mansour, A. Imad, "Effect of Temperature on Microstructure and Fracture Mechanisms in Friction Stir Welded Al6061 Joints", *Journal of Materials Engineering and Performance*, 2017, Volume 26, Issue 6, Pages 2542-2554.
- [51] R. F. Hamade, G. Ayoub, Z.G El Chlouk, G.T. Kridli, "Intermetallic Compound Formation in Al/Mg Friction Stir Welded (FSW) Butt Joints", *ASME International Mechanical Engineering Congress and Exposition, Proceedings (IMECE)*, 2014, 10.1115/IMECE2014-37213.
- [52] M. Raturi, A. Garg, A. Bhattacharya, "Joint Strength and Failure Studies of Dissimilar AA6061-AA7075 Friction Stir Welds: Effects of Tool Pin Process Parameters and Preheating", *Engineering Failure Analysis*, 2019, Volume 96, Pages 570-588.
- [53] R. Beygi, M. Zarezadeh Mehrizi, D. Verdera, A. Loureiro, "Influence of Tool Geometry on Material Flow and Mechanical Properties of Friction Stir Welded Al-Cu Bimetals", *Journal of Materials Processing Technology*, 2018, Volume 255, Pages 739-748.

- [54] S. Zhao, J. Ni, G. Wang, Y. Wang, Q. Bi, Y. Zhao, X. Liu, "Effects of Tool Geometry on Friction Stir Welding of AA6061 To TRIP Steel", *Journal of Materials Processing Technology*, 2018, Volume 261, Pages 39-49.
- [55] R. A. Gite, P. K. Loharkar, R. Shimpi, "Friction stir welding parameters and application: A review", *Materials Today: Proceedings*, 2019.
- [56] L Gao, H. Sun, X. Ni, M. Fang, T. Lin, "Effects Of 16-Bit CT Imaging Scanning Conditions for Metal Implants on Radiotherapy Dose Distribution", *Oncology Letters*, 2018, Volume 15, Issue 2, Pages 2373-2379.
- [57] J. Summerscales, "Non-Destructive Testing of Fibre-Reinforced Plastics Composites", Volume 2, 1990, chapter 4.2.4: Resolution, London, Elsevier applied science, Pages 208-209.
- [58] Xin-Ye N, Liugang G, Mingming F, Tao L. "Application of Metal Implant 16-Bit Imaging: New Technique in Radiotherapy". *Technology in Cancer Research and Treatment*, 2016, Volume 16, Issue 2, Pages 188-194.
- [59] S.A. Bolliger, L. Oesterhelweg, D. Spendlove, S. Ross, M.J. Thali, "Is Differentiation of Frequently Encountered Foreign Bodies in Corpses Possible by Hounsfield Density Measurement?", *Journal of Forensic Sciences*, 2009, Volume 54, Issue 5, Pages 1119-1122.

